The variable magnetic field of V889 Her and the challenge of detecting exoplanets around young Suns using Gaussian process regression

E. L. Brown [1,2]★ S. C. Marsden [1] S. V. Jeffers,[3] A. Heitzmann [1,4] J. R. Barnes[5] and C. P. Folsom[6]

[1]*Centre for Astrophysics, University of Southern Queensland, Toowoomba, QLD 4350, Australia*
[2]*School of Access Education, Central Queensland University, Cairns, QLD 4870, Australia*
[3]*Max Planck Institut for Solar System Research, Justus-von-Liebig-Weg 3, D-37077 Göttingen, Germany*
[4]*Observatoire Astronomique de l'Université de Genève, Chemin Pegasi 51, CH-1290 Versoix, Switzerland*
[5]*Department of Physical Sciences, The Open University, Walton Hall, Milton Keynes MK7 6AA, UK*
[6]*Tartu Observatory, University of Tartu, Observatooriumi 1, Tõravere 61602, Estonia*

ABSTRACT

Discovering exoplanets orbiting young Suns can provide insight into the formation and early evolution of our own solar system, but the extreme magnetic activity of young stars obfuscates exoplanet detection. Here we monitor the long-term magnetic field and chromospheric activity variability of the young solar analogue V889 Her, model the activity-induced radial velocity variations, and evaluate the impacts of extreme magnetism on exoplanet detection thresholds. We map the magnetic field and surface brightness for 14 epochs between 2004 and 2019. Our results show potential 3–4 yr variations of the magnetic field that evolves from weak and simple during chromospheric activity minima to strong and complex during activity maxima but without any polarity reversals. A persistent, temporally varying polar spot coexists with weaker, short-lived lower-latitude spots. Due to their different decay time-scales, significant differential rotation, and the limited temporal coverage of our legacy data, we were unable to reliably model the activity-induced radial velocity using Gaussian Process regression. Doppler Imaging can be a useful method for modelling the magnetic activity jitter of extremely active stars using data with large phase gaps. Given our data and using Doppler Imaging to filter activity jitter, we estimate that we could detect Jupiter-mass planets with orbital periods of ∼3 d. A longer baseline of continuous observations is the best observing strategy for the detection of exoplanets orbiting highly active stars.

Key words: planets and satellites: detection – stars: individual: V889 Her – stars: magnetic field.

1 INTRODUCTION

Young solar analogues show extreme magnetic activity that contrasts against the solar case, yet our Sun is thought to have behaved similarly during its infancy. By studying the magnetism of young solar analogues, we can look back at the Sun's possible early main sequence life and see how the conditions would have been within our own space environment. The detection of exoplanets around these stars could also give insight into the formation and early evolution of planetary systems around stars like our own, making young solar analogues important targets for both magnetic activity studies and in the search for exoplanets.

Today's Sun undergoes ∼ 22 yr magnetic cycles, wherein the large-scale magnetic field polarity reverses twice (every ∼ 11 yr) and between polarity reversals the magnetic field is converted from a dipolar, poloidal structure at magnetic minima, to a slightly more toroidal and complex geometry at magnetic maxima (DeRosa, Brun & Hoeksema 2012). The emergence of magnetic flux at the solar surface manifests in the growth and decay of dark spots, bright faculae, and plages throughout an 11 yr 'spot cycle' and also gives rise to a chromospheric activity cycle that is measurable using the

emissions in the cores of the chromospheric Ca II H and K spectral lines (Wilson 1978). Solar-like magnetic cycles have been identified in three other mature Sun-like stars based on periodic reversals of the large-scale magnetic field polarity that coincide with chromospheric activity cycles; 61 Cyg A (1.3–6 Gyr, K5V, ∼ 14 yr magnetic cycle; Boro Saikia et al. 2016, 2018), τ Boo (0.9 Gyr, F8V, ∼ 240 d cycle; Fares et al. 2009; Mengel et al. 2016; Jeffers et al. 2018), and HD 75 332 (1.88 Gyr, F7V, ∼ 1.06 yr cycle; Brown et al. 2021).

Young solar-type stars have shown comparatively chaotic magnetic behaviour, with magnetic fields that are an order of magnitude or more stronger than those seen in mature stars, often multiple coexisting activity cycles (Oláh et al. 2016; Boro Saikia et al. 2022; Jeffers et al. 2022) and polarity reversals that do not necessarily correspond to chromospheric activity cycles (Boro Saikia et al. 2022). One of the closest young solar-type stars, the ∼ 0.5 Gyr old (Barnes 2007) K2 dwarf ε Eridani, potentially alternates between chaotic and cyclic variability (Metcalfe et al. 2013; Petit et al. 2021), and the results from Jeffers et al. (2022) are consistent with a dynamo of two cycles where the shorter 3 yr cycle is a modulation of the longer 13 yr cycle. Young solar-type stars typically show strongly toroidal and axisymmetric magnetic fields (See et al. 2016; Folsom et al. 2018) compared to the Sun's dominantly poloidal magnetic field, with the most rapidly rotating main-sequence stars often showing strong rings of azimuthal field around the rotational axis (e.g. Marsden et al. 2006;

★ E-mail: emma.brown@usq.edu.au
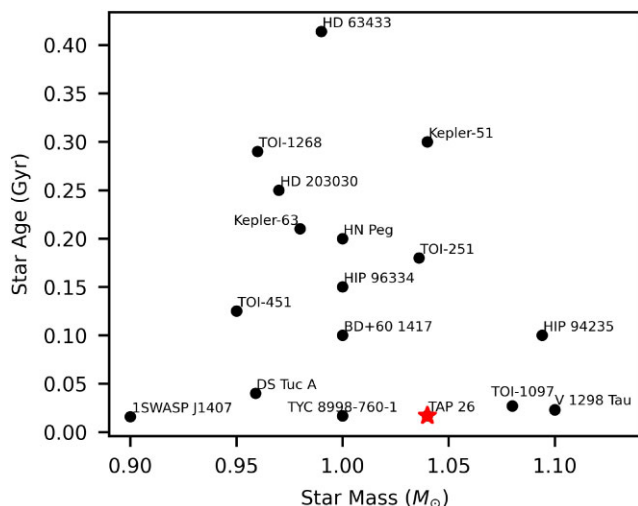
Figure 1. Age versus mass for planet-hosting stars with masses within 10 per cent of $M_\odot$ and ages below ~ 500 Myr. Only the star TAP26 (red) has had an exoplanet detected using only stellar RVs. For the remaining stars (black) exoplanets were detected using transits, direct imaging, or astrometry. Data taken from The Extrasolar Planets Encyclopaedia[1].

Jeffers & Donati 2008; Jeffers et al. 2011). Tomographic imaging of surface temperature contrasts, known as Doppler Imaging (DI), reveals large polar spots, or collections of spots, on young stars that are sustained for many years, in addition to comparatively short-lived low- to mid-latitude spots (e.g. Marsden et al. 2006; Jeffers & Donati 2008; Jeffers et al. 2011; Lehtinen et al. 2022). This is in stark contrast to the Sun, where spots are restricted to low latitudes, cover only 0.3–0.4 per cent of the solar surface at any time (Solanki & Unruh 2004) and last only days to months.

The extreme magnetic activity of young stars impacts on the ability to detect exoplanets using the radial velocity (RV) method, which is an important adjunct to other exoplanet detection techniques because it places unique constraints on the planetary mass. Exoplanet detection using the RV method relies on identifying Doppler shifts in stellar spectral lines to measure small changes in the RV of the star that are induced by orbiting objects. Magnetic activity complicates the detection of true Doppler shifts because spots and bright regions cause asymmetries in spectral line profiles that shift the line centre as they rotate in and out of view. These line shifts result in apparent, quasi-periodic RV variations with amplitudes up to hundreds of $\mathrm{m\,s^{-1}}$, which can obscure or even mimic the RV signatures of exoplanets (Barnes, Jeffers & Jones 2011; Jeffers et al. 2014; Nava et al. 2020). Other magnetic activity signatures, including a net convective blueshift across the stellar disc (Meunier, Desort & Lagrange 2010) and unresolved magnetic spots (Lisogorskyi et al. 2020), can each impart RV amplitudes as large as $10\,\mathrm{m\,s^{-1}}$, with this alone dwarfing the stellar RV signatures of planets up to $20\,M_\oplus$.

Young solar analogues make particularly difficult targets in the search for exoplanets, being near-solar mass, which makes true exoplanet RV signatures small, and highly active, making activity-induced RV amplitudes large. However, Jeffers et al. (2014) predicts that hot Jupiters (HJs) can be detected for young G and K dwarfs if they are observed over a sufficient time-base of 100 epochs. So far, for stars with masses within 10 per cent of $M_\odot$ and ages up to 500 Myr, shown in Fig. 1, only one has had an exoplanet detected using the RV method alone.

Methods to model and filter activity-induced RVs, such as the popular method of Gaussian Process Regression (GPR) and the 'DI' approach (see Section 3), have mostly been applied to near-solar mass stars with low-to-moderate levels of magnetic activity (e.g. Haywood et al. 2014; Heitzmann et al. 2021). GPR has also been tested against simple simulated spot patterns (Perger et al. 2021), but the reality is that young solar analogues have more complex spot topologies, with both long-lived polar spots and rapidly varying lower-latitude features (e.g. Marsden et al. 2006; Şenavcı et al. 2021; Willamo et al. 2022b). Heitzmann et al. (2021) tested the techniques of DI and GPR on the moderately active, 17–32 Myr, $1.3\,M_\odot$ G2 dwarf HD 141943, using legacy observations from the non-stabilized University College London Echelle Spectograph (UCLES[2]) at the Anglo Australian Telescope (AAT). They found GPR to be the more successful technique that was able to recover synthetic planetary signals with semi-amplitudes $\geq 100\,\mathrm{m\,s^{-1}}$ (i.e. a $1\,M_{\mathrm{Jup}}$ planet with orbital period of 5 d, for HD 141943). However, the spot pattern in HD 141943 that consists of low- and high-latitude features with similar strengths and area coverage, still contrasts against the intense polar spots that are ubiquitous among the most active young Suns and their significantly weaker low-latitude features. For active, low-mass stars, such as the $0.344\,M_\odot$, M3.5 dwarf EV Lac (Jeffers et al. 2022), the use of low-resolution DI activity models to remove the spot-induced RV component have been shown to improve the planet-mass sensitivity by a factor of three. The effectiveness of the DI and GPR methods for modelling the activity-induced RVs of highly active solar-mass stars has not yet been evaluated.

The young solar analogue V889 Her (HD 171488, G2V, Montes et al. 2001, 30–50 Myr old, $\sim 1.06\,M_\odot$, Strassmeier et al. 2003) is one of the brightest solar analogues that is rotating fast enough for active regions on its surface to be resolved using the technique of high-resolution DI. This makes it an important target to gain insight into the magnetic dynamos operating inside the most active Sun-like stars, and an ideal candidate to model activity-induced RVs using both the DI and GPR methods. V889 Her has been monitored spectropo-larimetrically with the NARVAL[3] spectropolarimeter at Télescope Bernard Lyot (TBL; at the Observatoire Pic du Midi, France, Aurière 2003), High Accuracy Radial velocity Planet Searcher polarimeter (HARPSpol) at the 3.6-m ESO telescope (La Silla Observatory, Chile, Snik et al. 2011), and the SEMEL polarimeter (SEMpol) at the AAT (Siding Springs, Australia, Semel, Donati & Rees 1993). This large data set provides an opportunity to study the long-term variability of magnetism in V889 Her and evaluate the impact of an extended baseline of observations on exoplanet detection capabilities for young solar analogues.

The large-scale magnetic field structure and brightness topology of V889 Her have been reconstructed in a number of previous studies (Strassmeier et al. 2003; Marsden et al. 2006; Järvinen et al. 2008; Jeffers & Donati 2008; Huber et al. 2009; Frasca et al. 2010; Jeffers et al. 2011; Willamo et al. 2022a), which have shown a strongly toroidal field geometry and a large spot (or collection of small, unresolved spots) that covers the visible pole of the star. The polar spot seems to have persisted from at least 1998 to 2011 (Strassmeier et al. 2003; Willamo et al. 2022a). Long-term photometric monitoring by Lehtinen et al. (2016) and Willamo et al. (2019b) has shown V889 Her to have a brightness cycle with a period of ~ 7–9 yr, but long-term S-index observations have not been available to detect a chromospheric activity cycle. Willamo et al. (2019b) did not find any consistent anticorrelation between the long-term brightness

Table 1. Summary of spectropolarimetric observations of V889 Her used for DI and ZDI. For each epoch, columns list the number of observations, the number of rotational cycles covered by the observations, the HJD of the first (HJD start) and last (HJD end) Stokes V observations, and the HJD corresponding to rotational cycle 0 for the epoch (close to the mid-point of the data, but an integer multiple of rotations from HJD=2453200). The final columns show the instrument that the observations were sourced with and indicate whether the data has been previously published. Full details for individual observations, including observations not used for tomographic imaging, are provided as supplementary materials. ∗ The 2005 May data originally published in Jeffers & Donati (2008) were not reanalysed here, but they have been included in Table 1 for completeness.

Map	Observations	Rotations	HJD start (+2453200)	HJD end (+2453200)	Mid HJD (+2453200)	Instrument	Ref.
2004 September	5	3.00	72.91	76.90	74.37	SEMpol	Marsden et al. (2006)
2005 May∗	10	7.61	322.45	332.35	326.50	MuSiCoS	Jeffers & Donati (2008)
2007 May	29	3.87	1042.47	1047.61	1045.14	NARVAL	Jeffers et al. (2011)
2007 November	14	3.81	1213.24	1218.31	1215.12	NARVAL	Jeffers et al. (2011)
2008 May	11	3.04	1413.46	1417.50	1415.65	NARVAL	Jeffers et al. (2011)
2009 May	12	3.05	1779.48	1783.53	1780.85	NARVAL	This study
2010 August	8	3.09	2218.58	2222.69	2220.42	HARPS	This study
2011 May 14–16	10	1.64	2496.76	2498.93	2497.97	HARPS	Willamo et al. (2022a)
2011 May 17–19	9	1.64	2499.74	2501.92	2500.62	HARPS	Willamo et al. (2022a)
2013 September	5	3.09	3347.49	3351.58	3349.22	HARPS	This study
2018 June	5	3.86	5095.43	5100.56	5098.19	NARVAL	This study
2018 July	12	8.20	5117.51	5128.40	5123.42	NARVAL	This study
2019 June	12	6.75	5456.43	5465.39	5460.74	NARVAL	This study
2019 July 10–19	10	6.78	5475.38	5484.39	5479.33	NARVAL	This study
2019 July 20–29	13	6.76	5485.42	5494.39	5489.95	NARVAL	This study

variations and spot filling factor (percent of the stellar surface covered in spots), as would be expected for a rapidly rotating star (Radick, Lockwood & Baliunas 1990), which they attributed to unreliable filling factor estimates. Willamo et al. (2019b) also found that V889 Her could have experienced a grand maximum in its magnetic activity between 2007 and 2017, based on a long-term minimum in brightness (if taken as a maximum in spot coverage/activity). Additionally, V889 Her has been monitored with NASA/MIT's Transiting Exoplanet Survey Satellite (*TESS*[4]). Potential transit signals have been flagged in the *TESS* data validation report summaries, with periods ranging between ~ 10 and 382 d, but none of these candidates have been elevated to a TESS Object of Interest (TOI).

In this work, we study the magnetic and chromospheric activity variability of V889 Her and model the activity-induced stellar RV shifts in an attempt to uncover the true stellar RV and search for RV shifts induced by exoplanets. The remainder of this paper is organized as follows: in Section 2, we describe the data used in this study. In Section 3, we outline the techniques used to reconstruct the large-scale magnetic field and brightness topology of V889 Her, extract precise RVs, chromospheric Ca II H&K activity, and model the activity jitter. In Section 4, we present the results of brightness and magnetic field modelling and analyse the long-term evolution of the large-scale magnetic field and brightness topology of V889 Her. The activity-induced RV variability is discussed in Section 5 as well as the challenges encountered in modelling the activity-induced RVs using GPR and DI to search for exoplanets. Finally, our conclusions are summarized in Section 6.

2 DATA

2.1 Spectropolarimetry with NARVAL, HARPSpol, and SEMpol

Our data include both previously published and new observations of V889 Her covering the period from 2004 May to 2019 July. We used observations from the NARVAL spectropolarimeter, HARPSpol

polarimeter in conjunction with the HARPS spectrograph, and SEMEL polarimeter coupled with UCLES. HARPS spectra have a resolution of $\sim 110\,000$ and spectral coverage from 3800 to 6900 Å compared to the data from NARVAL with a resolution of $\sim 65\,000$ and spectral coverage from 3700 to 11 000 Å, and UCLES spectra with a resolution of $\sim 70\,000$ and wavelength coverage 4400–6800 Å. The observations are summarized in Table 1, and further details are provided in the supplementary materials, with previously published data indicated where applicable.

Each of the instruments is configured for spectropolarimetry with the polarimeter mounted at the Cassegrain focus to split incoming circularly polarized (Stokes V) light into two orthogonally polarized beams, both of which are fibre-fed to the spectrograph and recorded on the detector. A single Stokes V observation consists of a series of two or four sub-exposures, where the positions of the orthogonally polarized beams are switched between sub-exposures. The Stokes V observation is determined by dividing sub-exposures with orthogonal polarization states, which removes spurious polarization signals to a first-order degree. Adding sub-exposures provides the unpolarized, Stokes I observation. For series of four sub-exposures, a 'Null' spectrum can also obtained by dividing spectra with identical polarization states, and this provides a measure of noise and a diagnosis of the reliability of the polarimetric measurement. For further information on this process, see Donati et al. (1997).

2.2 Data reduction and calibration

The observations were reduced and calibrated using the automated software package LIBRE-ESPRIT (based on ESPRIT, Echelle Spectra Reduction: an Interactive Tool, Donati et al. 1997). LIBRE-ESPRIT reduces the observations using bias and flat-field exposures averaged from series of exposures taken on the observing night. A first-order wavelength calibration is carried out using a Thorium–Argon arc lamp exposure. For NARVAL and UCLES spectra, the wavelength calibration is then further refined using telluric lines as RV references, as was first done by Donati et al. (2003). Telluric corrections are carried out for each observation individually, and this reduces the relative RV shifts to 100 m s^{-1} for UCLES spectra (Donati et al. 2003) and 30 m s^{-1} for NARVAL spectra (Moutou et al. 2007; Donati

et al. 2008). For HARPS spectra, we adopt an instrumental precision of 5 m s^{-1} based on Trifonov et al. (2020).

2.3 LSD spectral line profiles

We used the technique of Least-squares deconvolution (LSD; Donati et al. 1997) to derive high-signal-to-noise spectral line profiles from the observed spectra. LSD assumes that the spectral line asymmetries caused by magnetic activity are roughly equal across all spectral lines. Therefore, the entire observed spectrum of an active star can be thought of as a convolution of a 'mean' spectral line profile (i.e. the LSD profile) and the spectrum of the star when it is magnetically inactive. To model the spectrum of V889 Her, we used a line mask for a $T_{\text{eff}} = 5750\,K$, $\log g = 4.50$ and $\log(\text{M/H}) = 0.00$ star from Marsden et al. (2014). The line mask excluded lines with depth less than 10 per cent of the continuum and strong lines such as the chromospheric Ca II H&K lines. LSD was performed using the automated routine included in LIBRE-ESPRIT (Donati et al. 1997) and using the LSD normalization parameters from Marsden et al. (2014). Uncertainties for each of the LSD spectral pixels are scaled up from the spectral uncertainties as described in Wade et al. (2000a, b).

2.4 Photometry

V889 Her was observed by *TESS* in 2-min short-cadence integrations in sectors 26, 40, and 53. The Pre-search Data Conditioned Standard Aperture Photometry (PDCSAP) light curves are shown in Fig. A1, which show relative flux variations of up to $\sim 0.15 \times 10^5$ e s^{-1} that are assumed to be astrophysical.

V-band photometry obtained with the Tennessee State University T3 0.4 m Automatic Photoelectric Telescope (APT) located at Fairborn Observatory, Arizona, and spanning the years 1994–2018, was also previously published in Lehtinen et al. (2016) and Willamo et al. (2019b), and provided on VIZIER (Willamo et al. 2019a). The observations were made at a cadence of $\sim 1 - 3$ d. They were made differentially with respect to the comparison star HD 171 286 and the check star HD 170829, which is a constant star that is observed at the same time as the variable target to confirm that the comparison star has constant brightness. For further information on the acquisition and reduction of the differential photometry, see Lehtinen et al. (2016) and Willamo et al. (2019b).

3 ANALYSIS

3.1 Surface brightness and magnetic field mapping

3.1.1 Image reconstruction with ZDIPY

The tomographic imaging technique of DI and its derivative, Zeeman Doppler Imaging (ZDI), reconstruct the brightness contrasts and three-dimensional large-scale magnetic field across the stellar surface from series' of Stokes I and V LSD profiles, respectively. In this work, we used the ZDIPY code by Folsom et al. (2018), which is a python implementation of the extensively used C code described in Donati & Brown (1997) and uses a principle of maximum entropy image reconstruction, wherein the feature content of the reconstructed map is minimized. The resulting spot or magnetic map provides a lower limit for the amount of spot coverage or magnetic field strength and reliably recovers the fractions of different magnetic field components (Lehmann et al. 2019).

ZDIPY divides the stellar disc into equal-area tiles. For each tile, the Stokes I profile is modelled with a psuedo-Voigt profile (convolution of a Gaussian and Lorentzian, approximated according to Humlíček

1982), which is a more realistic approximation of the Stokes I profile compared to a Gaussian (Folsom et al. 2018). The Stokes V profile is derived using the weak-field approximation (Donati et al. 1997). The radial, azimuthal, and meridional magnetic field components are each represented as a series of spherical harmonics, with the order of the harmonic expansion limited by a factor l_{max} that is related to the complexity of the magnetic field (e.g. $l = 1$ for a dipolar field, $l = 2$ for quadrupolar field etc.). The full, disc-integrated line models are derived by summing the contributions of all tiles across the stellar surface. The contribution of each tile is scaled by its projected area and relative Doppler shift, taking into account the impact of limb darkening. The brightness or magnetic field (depending on which is being fitted) in each tile is iteratively varied, and the disc-integrated model computed. A model surface brightness or magnetic field map is simultaneously reconstructed from the model line profiles for each iteration, using a principle of maximum entropy image reconstruction, wherein the image feature content is minimized (Donati et al. 2006). The final maximum entropy map is that which achieves a target reduced-χ^2 fit to the observations. We used a target reduced-χ^2 value of 0.1 for Stokes I fitting, and 0.9 for Stokes V fitting (which is just below the noise level). It is usual to overfit the Stokes I line profiles because the signal-to-noise ratio for the LSD Stokes I profiles is underestimated (Wade et al. 2000a, b; Petit, Donati & Collier Cameron 2004a).

ZDIpy is capable of modelling the stellar surface brightness using a 'filling factor' or spot-only approach, whereby the star is modelled as a quiet surface (relative brightness = 1) with dark regions (relative brightness < 1), or the surface can be modelled as a combination of bright (relative brightness > 1) and dark (relative brightness < 1) regions. The spot-only approach has been used in all previous spot studies of V889 Her (Strassmeier et al. 2003; Marsden et al. 2006; Järvinen et al. 2008; Jeffers & Donati 2008; Huber et al. 2009; Frasca et al. 2010; Willamo et al. 2019b, 2022a) so here we use both methods to compare the resulting spot maps and determine if bright features like faculae are negligible in the DI analysis. Brightness mapping is a somewhat simplified approach compared to temperature mapping; in brightness mapping each surface pixel has a relative brightness, while in temperature mapping each pixel has a spot and a quiescent photosphere temperature, as well as a filling factor for the portion of the pixel covered by spots (e.g. Collier Cameron 2001). In a single line analysis, this spot temperature and filling factor are effectively degenerate, an issue that brightness mapping sidesteps by using a simplified model with only one free parameter per pixel. In brightness mapping spots are assumed to only produce changes in line shape, not equivalent width. Thus, the reconstructed brightness maps are essentially only sensitive to variations in the LSD profile shapes, not equivalent widths.

ZDIpy can model the magnetic field with or without taking into account a brightness map. When a brightness map is used as input for the magnetic field inversion, the code adjusts the inversion to account for the suppression of magnetic flux in dark regions. We tested our magnetic inversions when using spot-only and spot + bright maps as input and found no significant difference in the recovered magnetic field. The magnetic maps presented in our results take the spot-only maps as input.

ZDIpy can account for differential rotation of surface features using a solar-like differential rotation law:

$$\Omega(\theta) = \Omega_{\text{eq}} - d\Omega \sin^2 \theta, \tag{1}$$

where $\Omega(\theta)$ is the angular rotation rate at a latitude θ, Ω_{eq} is the angular rotation rate at the equator and $d\Omega$ the difference in rotation

Table 2. Stellar and line-model parameters for DI and ZDI.

Stellar parameters	
T_{eff} (K)	5769[a]
R ($R_\odot$)	1.09[b]
Age (Myr)	30–50[b]
Spectral type	G2V[c]
log g (dex)	4.30[a]
Solar line model parameters	
λ (nm)	580[d]
Gaussian width ($\sqrt{2}\sigma$, km s^{-1})	2.41
Lorentzian width (half-width at half-maximum, km s^{-1})	1.98
Effective Landé factor	1.22[d]
Limb darkening coefficient	0.66[e]
Derived DI/ZDI parameters	
RV	see Table B1
$v \sin i$ (km s^{-1})	37.5 ± 0.5
P_{rot} (d)	$1.328^{+0.012}_{-0.011}$
dΩ (rad d^{-1})	0.319 ± 0.114
Inclination angle (°)	60 ± 5
l_{max}	18

[a] Luck (2018); [b] Strassmeier et al. (2003); [c] Montes et al. (2001); [d] Marsden et al. (2014); [e] Gray (2005).

rate between the equator and the poles (i.e. the differential rotation rate), all measured in rad d^{-1}.

Table 1 provides a summary of the spectropolarimetric observations organized into 14 epochs, each with a sufficient number of observations (at least 5) and adequate rotational phase coverage to map the stellar surface using DI and ZDI. The time-spans covered by the data subsets range from 1.64 rotation cycles ($\sim$ 3 d) in 2011 May 14–16 and 2011 May 17–19, through to 8.20 rotational cycles ($\sim$ 11 d) in 2018 July. Even when adopting significant differential rotation in our models, we found that we needed to split the 2011 May data into small subsets to achieve a good fit of the ZDI model to the observations, consistent with Willamo et al. (2022a) and the rapid surface evolution seen in the *TESS* light curve for Sector 40 in Fig. A1. This suggests that field evolution occurs rapidly on a time-scale as short as $\sim$3 d. For other epochs, such as 2018 July through to 2019 July, we were able to easily fit to the noise level with much longer series' of observations. The difference could be due to the higher resolution of the HARPSpol data, which may better recover the evolution of small-scale magnetic features, or possibly evolution of the stellar surface is not always as rapid as in 2011 May. We tested shorter series' of observations for 2018 June through to 2019 July but did not find that this significantly affected the results we report in Section 4.3. The magnetic and bright/dark features in our reconstructions for these epochs (Figs B1 to B3) do not show any obvious smearing that would suggest more rapid evolution of the magnetic field was occurring.

3.1.2 Stellar and model parameters

We modelled the Stokes *I* LSD line profiles using a solar line model with the properties shown in Table 2. The line-model parameters were fitted to a solar LSD profile, derived from a NARVAL spectrum of sunlight reflected from the moon. The line model is considered to be a suitable approximation for V889 Her, which has a similar spectral type to the Sun.

ZDIPY also requires input of the centre-of-mass RV of the star, its line-of-sight projected rotational velocity ($v \sin i$), inclination angle (i), equatorial rotation period (P_{eq}), and rate of differential rotation (dΩ). To select appropriate parameters, we used a process of χ^2 minimization, whereby we iteratively varied input parameters and recomputed the stellar model to identify the parameters that minimize the reduced-χ^2 fit to the observations.

For the RV, $v \sin i$ and inclination angle, we varied the parameters individually and fitted to the Stokes *I* LSD line profiles. The best-fitting RV fluctuated slightly between epochs, as shown in Table B1. It is not clear if these long-term RV shifts are true centre-of-mass fluctuations, but to optimize the DI and ZDI models, we have adopted the best-fitting RV on an epoch-to-epoch basis. The best-fitting $v \sin i$ and inclination angle are shown in Table 2 and are reasonably consistent with previous work (Strassmeier et al. 2003; Marsden et al. 2006; Jeffers & Donati 2008; Jeffers et al. 2011; Willamo et al. 2019b). The inclination angle is typically the most difficult parameter to constrain using χ^2 minimization. The 60 ± 5° we derived using χ^2 minimization is consistent within the error bars with an inclination angle of 64.5° derived using our measured equatorial rotation period and $v \sin i$, adopting a stellar radius of 1.09$R_\odot$ (Strassmeier et al. 2003) and by assuming solid-body rotation. As discussed by Willamo et al. (2022a), the possible detection of transiting exoplanets by *TESS* suggests a higher inclination angle if we assume that the planet's orbital axis is aligned with the star's axis of rotation. We tested our magnetic field and surface brightness reconstructions using a greater inclination angle of 85° and the models converged at much higher reduced-χ^2 values, indicating a poor fit of the model to the data. Given that none of the potential transits detected by *TESS* have been elevated to a TOI, we have adopted the best-fitting inclination angle of 60° for ZDI.

To determine the optimal equatorial rotation period and rate of differential rotation, we varied the parameters together according to equation (1). We fit this using the Stokes *V* profiles, since V889 Her shows more latitudinal distribution of magnetic features compared to spots, which are mostly observed over the pole both in our study and in previous work (Strassmeier et al. 2003; Marsden et al. 2006; Jeffers & Donati 2008; Jeffers et al. 2011; Willamo et al. 2019b, 2022a). The HJD corresponding to rotational cycle zero (i.e. the date where the magnetic field is assumed to be unsheared by differential rotation) .is given in Table 1 for each epoch.

In Fig. 2 (left-hand panel), we show the reduced-χ^2 landscape for our 2007 May data set, which has excellent phase coverage for tracing the differential rotation of magnetic features (29 observations across 3.87 rotational cycles). The model can be fitted to the noise level, which suggests that the stellar surface is not significantly evolving during the observations. In Fig. 2, the colour represents the reduced-χ^2 fit (with a fixed entropy) for each combination of P_{eq} and dΩ, and we also show the 1-σ and 2-σ uncertainty contours around the best-fitting values. In the right-hand panel of Fig. 2, we show the 1-σ uncertainty regions for several of our epochs that have adequate phase coverage to measure differential rotation. The best-fitting rotational parameters derived for each epoch vary, which is consistent with the varying parameters, derived across previous studies of V889 Her. Given that the uncertainty regions for these epochs overlap, roughly forming a larger uncertainty ellipse, we take these apparent epoch-to-epoch variations as an indication that the uncertainty of our measurement is larger than suggested by the individual 1-σ uncertainty regions, similar to Marsden et al. (2007). For all our models, we have adopted the median equatorial rotation period of P_{eq} =1.328 d and median rotational shear of dΩ = 0.319 rad d^{-1}.
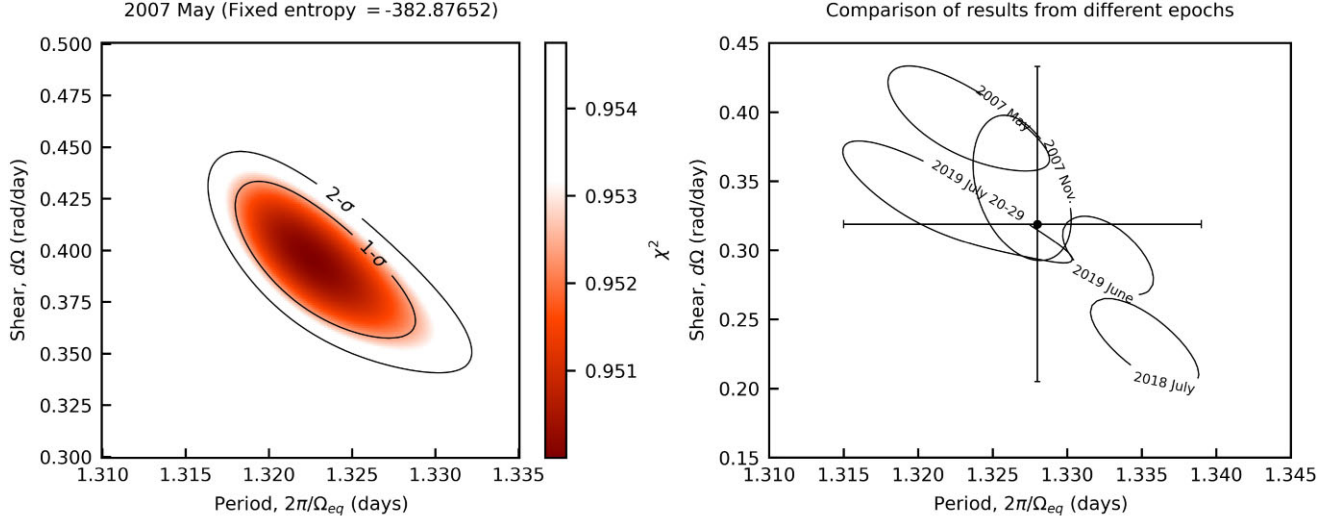
Figure 2. Left: Example plot of the reduced-χ^2 landscape when fitting to the Stokes V profiles from 2007 May. The darkest red region represents the best-fitting combination of the equatorial rotation period (d) and rotational shear (rad d^{-1}). The 1σ and 2σ contours are also shown. Right: The 1σ contours from multiple epochs are plotted on top of each other. The mean and uncertainty of the adopted equatorial period and rotational shear are also shown with the cross-hair.

Finally, ZDIPY uses a maximum degree of harmonic expansion, l_{max}, to control the complexity of the magnetic field reconstruction. We tested increasing l_{max} and found there to be no improvement in the reduced-χ^2 fit nor any obvious changes in the reconstructed magnetic field geometry for $l_{max} > 18$; therefore, we have adopted $l_{max} = 18$.

3.1.3 Uncertainty analysis

We tested the sensitivity of our magnetic field and brightness models to changes in the P$_{eq}$, dΩ, RV and $v \sin i$ within their uncertainties. The variation bars shown in Table B1 for the DI and ZDI results relate to the changes in the model outputs while we simultaneously varied the input parameters within their uncertainties. The largest impact comes from variations in the $v \sin i$ which relates to the rotational broadening of the line profile. Changes in the $v \sin i$ are reflected as significant increases in spot coverage.

3.2 Chromospheric activity

We measured chromospheric activity for each RV-corrected observation (Section 3.4) using the S-index, which is a measure of the excess flux in the cores of the Ca II H and K absorption lines that is related to non-thermal heating of the chromosphere. S-index observations carried out with NARVAL and HARPS were converted to the common Mount Wilson scale (Wilson 1978) using the formula

$$S = \frac{aF_H + bF_K}{cF_{R_{HK}} + dF_{V_{HK}}} + e \tag{2}$$

where F_H and F_K are the fluxes in two triangular bandpasses centred on the cores of the Ca II H and K lines (3968.469 and 3933.663 Å) with widths of 2.18 Å (at the base), and $F_{R_{HK}}$ and $F_{V_{HK}}$ are the fluxes in two rectangular 20 Å bandpasses centred on the continuum either side of the H&K lines at 3901.07 and 4001.07 Å. The calibration coefficients a, b, c, d, and e for NARVAL data are available in Marsden et al. (2014), and the coefficients for HARPS data were taken from Gomes da Silva et al. (2020). The wavelength coverage of UCLES spectra do not allow for the S-index to be calculated.

3.3 Longitudinal magnetic field

The longitudinal magnetic field, B_l (G), is the line-of-sight magnetic field strength averaged over the visible stellar surface. For each RV-corrected observation, we measured B_l directly from the LSD profiles using the equation

$$B_l = -2.14 \times 10^{11} \frac{\int v V(v) dv}{\lambda g c \int [1 - I(v)] dv} \tag{3}$$

where $V(v)$ and $I(v)$ are the Stokes V and I LSD profiles, respectively, λ (580 nm) is the central wavelength of the LSD profile, g is the mean Landé factor (1.22), c is the speed of light in km s^{-1}, and v is velocity in km s^{-1} (Donati et al. 1997). We integrated over a velocity domain of -52–52 km s^{-1} with respect to the line centre to include the entire Stokes V polarization signal while minimizing noise. B_l measurements for each observation are provided as supplementary materials, with error bars determined by propagating the uncertainties computed during the reduction process for each spectral bin of the normalized spectrum through equation (3).

3.4 Precise RVs from LSD profiles

RVs measured from LSD spectral line profiles can be used to detect exoplanets, as demonstrated by Lienhard et al. (2022). We measured precise RVs for each individual observation by computing the first-order moment (FOM) of the continuum-normalized Stokes I LSD profile, according to

$$RV = \frac{\int (I_c - I(v)) v \, dv}{\int (I_c - I(v)) dv} \tag{4}$$

where I_c is the continuum intensity level, $I(v)$ is the intensity at a velocity v (km s^{-1}), and the integral is computed over a velocity range of -76–30 km s^{-1} in the heliocentric corrected frame. RVs for each individual observation are included in Table 1 of the Supplementary Materials. To determine the uncertainties in each RV measurement, we derived the uncertainty in the FOM by propagation of the uncertainties in the LSD line profile and added this in quadrature to the instrumental uncertainty from Section 2.2.

3.5 Photometric rotation period

The *TESS* light curves in Fig. A1 show clear rotational modulation related to brightness contrasts on the stellar surface. The light curve from sector 40 is particularly interesting, with the shape of the modulation changing significantly over ~ 15 d. The beating and sub-period structure in sector 40 is likely due to rapid evolution of ≥ 2 spots at different latitudes and the presence of significant differential rotation. We measured periods of 1.329 d through to 1.432 d for the modulations using the Lomb–Scargle periodogram. These are in reasonable agreement with our adopted equatorial rotation period and differential rotation rate in Table 2 and would reasonably correspond to the differentially rotating equatorial and polar spots.

3.6 Photometry smoothing

The APT differential photometry shows both rotational modulation and significant long-term variability, as has been previously discussed by Lehtinen et al. (2016) and Willamo et al. (2019b). We used a moving average to smooth out short-term variations and observe longer-term periodicities. Willamo et al. (2019b) previously took the mean photometric magnitude from a sliding 30 d window of observations, with a minimum of 14 observations required to be in the window. For the same data presented by Willamo et al. (2019b), we have used a more vigorous smoothing approach to search for brightness fluctuations on a time-scale of months to years, taking the mean magnitude from a 180 d sliding window which is similar in length to an observing season. The raw and smoothed data are shown in Fig. 5, and we discuss this further in Section 4.3.

3.7 Activity filtering and an RV search for exoplanets

The stellar RVs we measured from spectral line profiles are a superposition of true centre-of-mass RVs, and apparent spectral line-centre shifts caused by surface temperature contrasts (i.e. dark spots and bright regions) that change the line shape. We modelled these activity-induced RV fluctuations using two methods, the DI method and GPR, and searched for underlying periodic RV fluctuations that could indicate the presence of a planetary companion.

3.7.1 The 'DI method'

The DI method (e.g. Donati et al. 2014; Barnes et al. 2017) makes use of the synthetic Stokes *I* profiles that were generated to model the surface brightness topology of V889 Her (Section 3.1.1), and which give an estimate of apparent RV shifts related to surface brightness features. We measured RVs from both the raw and synthetic LSD profiles using the method described in Section 3.4, and then subtracted the synthetic RVs directly from the raw RVs. We used the generalized Lomb–Scargle periodogram (Lomb 1976; Scargle 1982; Zechmeister & Kürster 2009) to search for periodicities in the residual RVs and assessed the significance of peaks using false alarm probabilities (FAPs) calculated using a bootstrap re-sampling approach. Following Zechmeister, Kürster & Endl (2009), we generated 10 000 re-sampled data sets, for each set retaining the timestamps of the RV observations and assigning randomized RV values (with replacement) to each time stamp. We then used the GLS periodogram to find the highest-power peak for each re-sampled data set and used the maximum peak heights from all 10 000 data sets as an estimate of the probability distribution of power maxima. The power values that are above 99.9 per cent and 99 per cent of all power maxima are taken as the 0.1 per cent and 1 per cent FAPs, respectively.

Table 3. Priors adopted for each of the hyperparameters in equations (5) and (6). $\mathcal{U}$ and $\mathcal{G}$ represent Uniform and Gaussian distributions. Bracketed values are the minimum and maximum for uniform priors, and the mean and standard deviation for Gaussian priors. RV_{max} is the maximum unsigned RV, σ_{RV} is the standard deviation of the RV, and T is the time-base of the data set.

Hyper-parameter	Prior
θ_1 (km s^{-1})	$\mathcal{U}$ (0, RV$_{max}$)
θ_2 (d)	$\mathcal{U}$ log(1.33, 100)
θ_3 (d)	$\mathcal{G}$ (1.33, 0.1)
K (km s^{-1})	$\mathcal{U}$ (0, 2RV$_{max}$)
P$_{orb}$ (d)	$\mathcal{U}$ (0, 0.5T)
Φ	$\mathcal{U}$ (0, 1)
RV$_N$ (NARVAL)	$\mathcal{G}$ (0, σ_{RV})
RV$_H$ (HARPS)	$\mathcal{G}$ (0, σ_{RV})
RV$_A$ (AAT)	$\mathcal{G}$ (0, σ_{RV})
σ_N	$\mathcal{G}$ (0, σ_{RV})
σ_H	$\mathcal{G}$ (0, σ_{RV})
σ_A	$\mathcal{G}$ (0, σ_{RV})

3.7.2 Gaussian process regression

The second method was to model the activity-induced RV shifts and their temporal evolution as a Gaussian process (GP). GPR treats the activity-related RVs as correlated Gaussian noise, where the covariance matrix, C, specifies the correlation between each pair of RV observations. We used the GPR implementation of Heitzmann et al. (2021), which follows Haywood et al. (2014), with each entry in the covariance matrix computed from the quasi-periodic kernel

$$C_{ij} = \theta_1^2 \cdot \exp\left[-\frac{(t_i - t_j)^2}{\theta_2^2} - \frac{\sin^2(\frac{\pi(t_i - t_j)}{\theta_3})}{\theta_4^2}\right] + (\sigma_i^2 + \sigma_s^2)\delta_{ij} \qquad (5)$$

where the hyperparameter θ_1 (kms^{-1}) is the semi-amplitude of the RV signal related to activity, θ_2 (d) is the decay parameter, taken to represent the typical lifetime of stellar surface features, θ_3 (d) is the recurrence time-scale of features ($\sim$ P$_{rot}$) and θ_4 is a smoothing parameter that indicates how complex the signal is within one period. We fixed θ_4 at 0.31 according to Perger et al. (2021), but we found that having a fixed or variable θ_4 made little difference to our findings in Section 5.3. The uncertainty in each data point, σ_i, and an extra uncorrelated noise parameter, σ_s, are added in quadrature and applied to the diagonal of the covariance matrix (i.e. the variance of the data). We also include an RV offset (RV$_o$) for each observing instrument. We fitted the GP to the raw RVs using the nested sampling Monte Carlo routine PYMULTINEST (Buchner et al. 2014), a PYTHON implementation of MULTINEST (Feroz, Hobson & Bridges 2009). Priors were taken from Table 3. In GPR, the rotational spot signal is allowed to change its amplitude and phase over time, which is physically motivated by the short-term changes in mid- to low-latitude spots on V889 Her. Given that the large polar spot on V889 Her is very long-lived, we set the priors for the decay parameter to trace the formation and decay of comparatively short-lived lower latitude features.

GPR can be used to search for exoplanets by also fitting an activity + planet model to the data, and using Bayesian model comparison to assess the significance of the activity + planet model over the activity-only model. The RV shifts due to an exoplanet in a circular orbit follow the equation

$$RV_{planet}(t) = K \sin\left(\frac{2\pi t}{P_{orb}}\right) - \Phi + 0.5 \qquad (6)$$

where RV$_{\text{planet}}$(t) is the RV shift at a time t (km s^{-1}), K is the RV semi-amplitude (km s^{-1}), P_{orb} is the orbital period (d), and Φ the orbital phase [0, 1]. The Bayesian evidence for each model was computed with the nested sampling MC algorithm during parameter fitting by integrating over all model parameter spaces according to equation (7)

$$Z = \int L(\theta)\pi(\theta) \, d^N\theta \tag{7}$$

where L(θ) is the likelihood and $\pi(\theta)$ the prior probability for the set of model parameters θ, and N is the number of model parameters. According to Trotta (2008), the activity + exoplanet model can be accepted over the activity-only model when the difference in the log of the Bayesian evidence is $\Delta \ln Z > 5$.

4 MAGNETIC FIELD AND BRIGHTNESS TOPOLOGY OF V889 HER

Table B1 provides a summary of results from the surface brightness and magnetic field mapping. The full set of surface brightness and magnetic field maps are provided in Figs B1 through to Fig. B3. The fits of the model Stokes *I* and *V* line profiles to the observations, and the measured RV, S-index and longitudinal magnetic field strength for each individual observation are also provided as supplementary materials.

4.1 Brightness maps

The bright+spot, and spot-only maps are all dominated by the presence of a large, slightly off-centre and long-lived polar spot (or multiple, unresolved small spots) that extends down to $40 - 50°$ latitude. This is consistent with all previous surface brightness models of V889 Her (Strassmeier et al. 2003; Marsden et al. 2006; Jeffers & Donati 2008; Jeffers et al. 2011; Willamo et al. 2019b, 2022a). The results also confirm the presence of lower-latitude spots in the visible hemisphere of V889 Her. Previous work by Marsden et al. (2006), Jeffers et al. (2011) and Willamo et al. (2019b) also showed small-scale dark features at the mid- to low-latitudes, whereas Jeffers & Donati (2008) did not find evidence for such spots in 2005 May to June using data from the MuSiCoS spectrograph (Baudrand & Bohm 1992; Donati et al. 1999) coupled with the TBL, which were unavailable for reanalysis in this work. This difference could be related to the slightly lower resolution of MuSiCoS spectra ($\sim$ 35000), or it could be that the lower-latitude spots are not always present, although all of our maps show at least weak low-latitude features. It is not clear from our data if there is a relationship between the strength of the polar spot and the existence of lower latitude features, but the mean spot coverage does show some correlation with the strength of the magnetic field, which we discuss further in Section 4.3.

Between the bright+spot and spot-only models, the most striking difference is that the bright+spot maps show weak but significant spot coverage in the 'southern' hemisphere of the star. Although there are likely to be spots on both hemispheres, it is not clear if the spots shown in the southern hemisphere are artefacts that compensate for the extensive bright regions in the spot+bright models. The spots in the southern hemisphere are reflected in Table B1 as a significantly larger spot coverage for the bright+spot models compared to the spot-only models. Although we found that the bright+spot models typically converged to lower χ^2 values compared to the spot-only models, this is to be expected for any model with a greater number of variables, and it is not clear which of the inversion techniques results in the most reliable spot model.

The percentage of the stellar surface covered in spots varies between 3.6 per cent in 2008 May and 7.3 per cent in 2011 May 14–19, for the spot-only models. Our spot map for 2004 Sept. is similar to that produced by Marsden et al. (2006) using the same data. They obtained a spot coverage of 5.5 per cent, which is in reasonable agreement with our 6.9 per cent in the spot-only model, considering that Marsden et al. (2006) used a different ZDI implementation from Brown et al. (1991) and Donati & Brown (1997).

4.2 Large-scale magnetic field maps

The magnetic field maps in Figs B1 through to Fig. B3 indicate a persistent wreath of positive azimuthal field that surrounds the visible pole of V889 Her at all epochs except 2008 May when the magnetic field is at its weakest. Although the weaker field shown in 2008 May may be partly related to the fairly sparse phase coverage of the data, there is similar phase coverage in 2010 August, whereas the recovered magnetic field is comparatively strong. Therefore we are confident that the changes in the field strength are not completely related to differences in the phase coverage of data across epochs.

At latitudes below $\sim 60°$ the azimuthal field shows mixed polarity regions that have low-to-moderate field strengths (compared to the positive polar wreath). From 2018 June toward the end of our data, the mid-latitudes become dominated by negative regions of azimuthal field, which form a second wreath surrounding the polar wreath. Similar double wreaths persisting over multiple years have been observed for other active stars, like the rapidly rotating K1 subgiant HR 1099 (Petit et al. 2004b), which has a rotation rate approximately 10 times the solar rotation rate (compared to ~ 20 times the solar rotation rate for V889 Her). Large-scale azimuthal wreaths have also been reproduced in magneto-hydrodynamoic (MHD) simulations of rapidly rotating Suns by Brown et al. (2011). The presence of such large-scale azimuthal magnetic structures at the stellar surface has been taken as an indication of a fundamentally different dynamo process operating in active stars, compared to that operating within the Sun (e.g. Donati et al. 2003).

In contrast to the azimuthal field, the radial field shows mixed polarities at high latitudes, consistent with previous observations of V889 Her by Marsden et al. (2006), Jeffers & Donati (2008) and Jeffers et al. (2011). The radial field over the visible pole and at high latitudes is dominantly negative for most epochs, including in 2011 May 14–15 and 2011 May 17–19, which is consistent with Willamo et al. (2022a). However, the radial field over the pole becomes dominantly positive in 2007 November, 2010 August, 2013 September, and 2019 June, as indicated by Fig. 3, which shows the fractional magnetic field strength as a function of latitude for each of the radial, azimuthal and meridional field components. The fractional magnetic field was calculated using the formula

$$F(\theta) = \frac{B(\theta)\cos(\theta)d\theta}{2} \tag{8}$$

where $F(\theta)$ and $B(\theta)$ are the fractional and average magnetic field strengths of each component at latitude θ, and $d\theta$ is the thickness of individual latitude bands. The switch to a dominantly positive radial field over the visible pole does not indicate a full polarity reversal, with the opposite hemisphere of the star remaining dominantly positive throughout all of our observations. Periods of singular large-scale polarity, where the large-scale magnetic field has the same polarity in both stellar hemispheres, have also been reproduced in the simulations of Brown et al. (2011) for rapidly rotating Suns.

Interestingly, the dominant field polarity of the meridional component over the pole also changes for 2007 November, 2010 August,
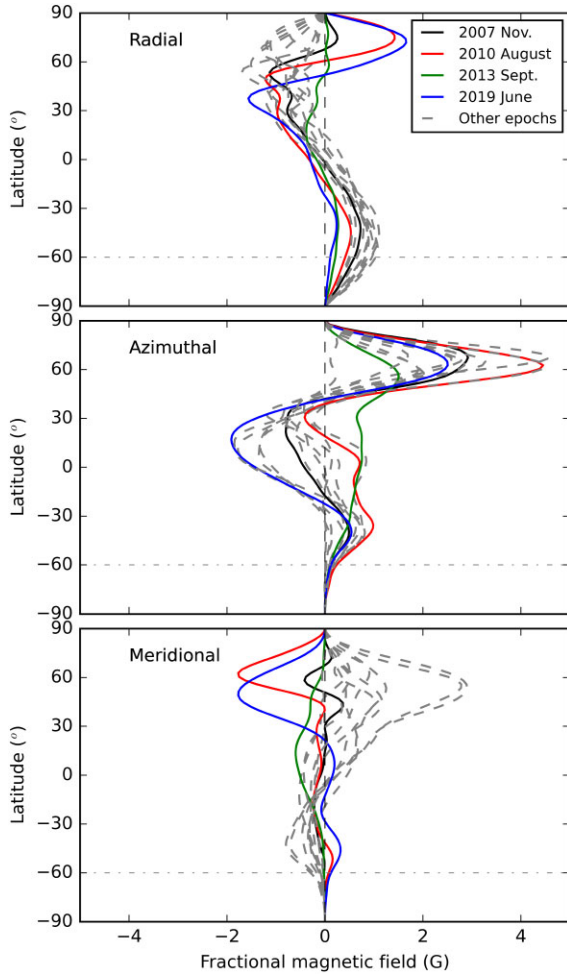
Figure 3. Fractional magnetic field strength per latitude band for the radial (top), azimuthal (middle), and meridional (bottom) field components. For epochs addressed in Section 4.2, the data are coloured, and the rest of the epochs are shown as dashed grey lines. The horizontal dashed line at $-60°$ latitude indicates the lower extents of our magnetic maps.

and 2013 September. The meridional field polarity even appears to reverse in the hidden hemisphere in 2019 June, but reverts back before 2019 July 10–19. The meridional field is the weakest field component, possibly because ZDI becomes less sensitive to low-latitude meridional fields with increasing stellar inclination (Donati & Brown 1997).

Our magnetic field reconstructions show a stronger magnetic field compared to previously published results from Marsden et al. (2006), who measured a mean field strength of ~ 30 G in 2004 Sept. compared to our ~ 87 G. One reason for this is that we have used different modelling approaches. ZDIPY is capable of fitting to the Stokes V profiles while taking into account the brightness image, so it can account for regions of reduced flux and increase the magnetic field accordingly. As shown in Fig. C1, magnetic models reconstructed in consideration of the brightness topology show considerably stronger magnetic structures, in particular the azimuthal polar wreath, when compared to a magnetic model that does not take into account the brightness topology at all. Conversely, the field strengths measured here for 2011 May 14–16 and 2011 May 17–19 are an order-of-magnitude smaller compared to those measured by Willamo et al. (2022a), potentially due to the use of different ZDI software.
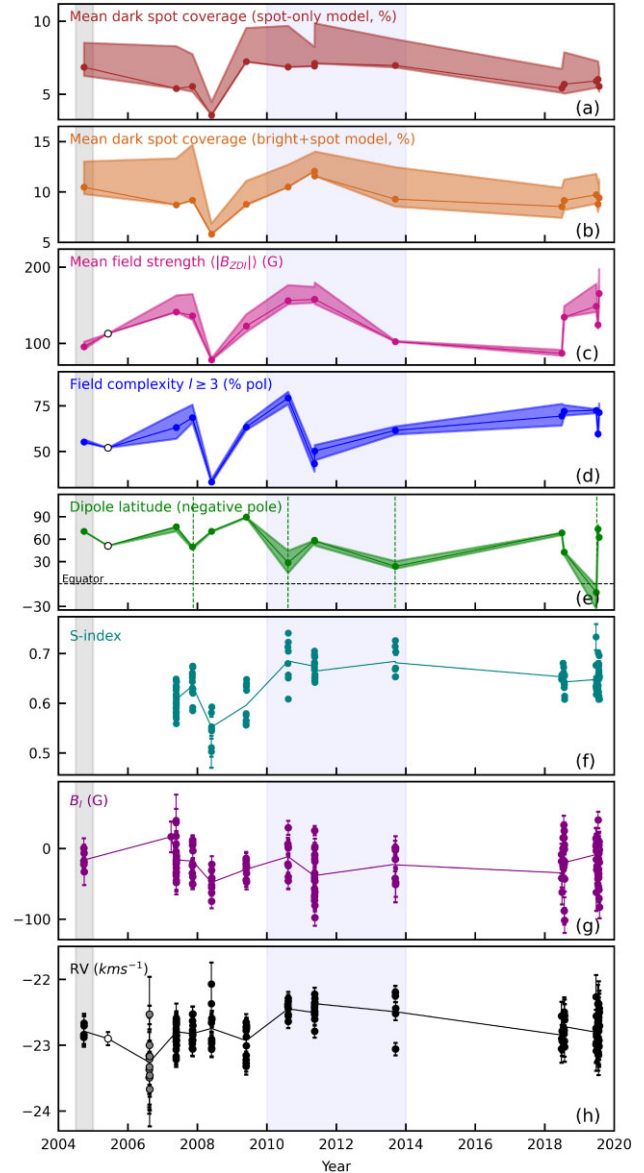
Figure 4. Time-series plots of the surface brightness properties, large-scale magnetic field parameters, and magnetic activity metrics for V889 Her between 2004 and 2020. From top to bottom, the axes show (a) mean spot coverage for spot-only models, (b) mean spot coverage for bright+spot models, (c) mean magnetic field strength from ZDI, (d) fraction of the poloidal field stored in octopolar and higher-order modes, (e) latitudinal location of the large-scale magnetic dipole (negative pole), with dashed vertical lines indicating possible reversal attempts, (f) chromospheric S-index, (g) surface-averaged longitudinal magnetic field strength, and (h) the radial velocity measured from the first-order moment of the observed LSD profile. The shaded regions for plots (a) through (e) indicate the sensitivity of our ZDI results to variations in the P_{eq} $(^{+0.012}_{-0.011}$ d), dΩ (±0.114 rad d^{-1}), $v \sin i$ (±0.5 km s^{-1}), and RV (see Table B1). In axes (f)–(h), solid lines join the mean values for each observational epoch. The grey and blue vertical shaded bands indicate data from UCLES and HARPS, respectively. Un-shaded data are from NARVAL. Additionally, in (c), (d), (e), and (h), the data shown with open circles were provided by the authors of Jeffers & Donati (2008; note that these data have no 'variation bars'). In (h), the grey filled circles are RVs from Frasca et al. (2010).
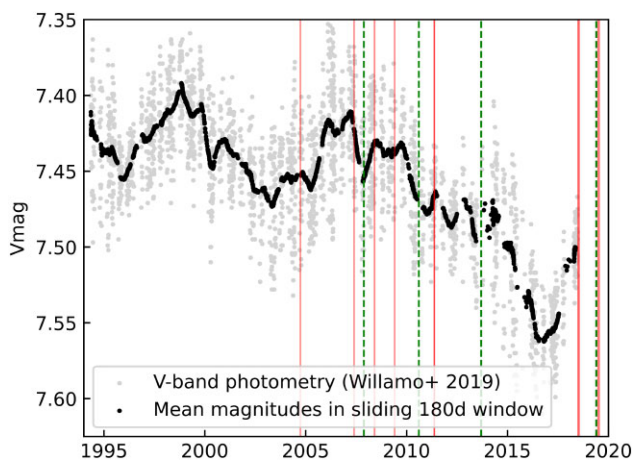
Figure 5. V889 Her brightness variations as shown by differential V-band photometric magnitudes taken between 1994 and 2018. The photometric data, originally published by Lehtinen et al. (2016) and Willamo et al. (2019b), are shown as light grey data points, and our moving 180 d averages are shown as black points. Green dashed vertical lines indicate the epochs of possible 'attempted reversals' in Fig. 4, and red vertical lines indicate all other ZDI epochs.

4.3 Long-term activity and magnetic field evolution

Fig. 4 compares key results from the surface brightness and magnetic field mapping to the chromospheric activity, surface-averaged longitudinal magnetic field strength and radial velocity of V889 Her for the period from 2004 to 2020. The variation bars on the magnetic field parameters in Fig. 4 were determined by varying the ZDI model input parameters within their uncertainties, and recomputing the brightness and magnetic maps. All of the trends in magnetic field properties that we discuss in this section are more significant compared to the uncertainty bars. We also show the results of our photometry smoothing in Fig. 5, where we used a moving 180 d average to smooth out short-term variations in surface brightness. We have drawn green vertical lines in Fig. 5 to indicate the epochs where the large-scale magnetic dipole latitude reaches local minima in Fig. 4. The synthesis of these data suggests that there are short-term, quasi-periodic magnetic field fluctuations in V889 Her, the first to be observed for such a young solar analogue.

Between 2007 May and 2011 May 14–16, V889 Her appears to undergo one full oscillation in terms of its magnetic field strength measured from ZDI. The chromospheric S-index and surface-averaged longitudinal magnetic field strength, B_l, correlate loosely with the field strength measured from ZDI, with both reaching local minima in 2008 May, and local maxima in 2010 August. We determined Pearson's correlation coefficients of 0.52 and 0.39, respectively for S-index and B_l data binned by epoch, with p-values (probability of finding a correlation where there is none) of 0.15 and 0.30. The magnetic maps also indicate that the field is simple during the magnetic and activity minima in 2008 May, with the fraction of magnetic energy stored in high-order modes ($l \geq 3$) at its lowest, while the poloidal field fraction and dipolar field strength are at maxima (Table B1). As the field strength and chromospheric activity grow toward maxima around 2010/2011, the dipolar component of the field decreases and higher-order components increase as the field structure becomes complex and dominantly toroidal. Our observations show the negative pole of the large-scale radial dipole dipping toward equator on two occasions during this period, in 2007 November and

2010 August. These epochs are also when the radial field becomes dominantly positive over the visible stellar pole in Fig. 3.

The transformation of the magnetic field during this 3–4 yr period has some similarities to the solar cycle, during which the Sun's magnetic field gains strength and is converted from simple and weak to complex and strong. A key aspect missing for V889 Her, at least in our observations, is the cyclic reversal of the large-scale magnetic dipole, which occurs at around magnetic maxima in the Sun and which regenerates the poloidal field but with opposite polarity. In V889 Her, the large-scale magnetic dipole instead approaches the equator around magnetic maxima, and then the poloidal field is regenerated with the same polarity as before. MHD simulations by Brown et al. (2011) have showed similar polarity reversal 'attempts' for a young Sun rotating at five times the solar rotation rate (compared to $\sim 20\times$ the solar rotation rate for V889 Her). The simulations showed that full reversals can occur in the 5Ω-rotating young Sun model, but not every time magnetic energies undergo a full oscillation. There were several failed polarity reversal attempts for each successful one. Further observations will be required to determine whether or not full reversals of the magnetic dipole of V889 Her are possible.

Although we cannot confirm the presence of any chromospheric activity cycles from our S-index data, at least two potential cycles appear to be present in the smoothed photometry in Fig. 5, which we would expect to relate to the formation and decay of spots in a rapidly rotating star such as V889 Her (Radick, Lockwood & Baliunas 1990). There is a long cycle of 7–9 yr that is clearly evident in the photometry between 1994 and 2007 and is consistent with the long-term cycle previously reported by Strassmeier et al. (2003), Lehtinen et al. (2016), and Willamo et al. (2019b). There are also short-term fluctuations in the photometry that occur as rapidly as every $\sim 1 - 1.5$ yr, around half the period of our observed magnetic field and chromosperhic activity fluctuation shown in Fig. 4. Interestingly, the magnetic field reversal attempts indicated by our magnetic maps each coincide roughly with local minima in the short-term photometric fluctuations. The fact that the polarity reversal attempts seem to follow photometric cycles supports the presence of repetitive magnetic fluctuations, even though our magnetic field maps have only captured a single fluctuation.

Jeffers et al. (2022) recently showed for ϵ Eri, which has coexisting ~ 3 and ~ 13 yr chromospheric activity cycles, that the magnetic flux generation and emergence follow the longer chromospheric activity cycle but are modulated by the shorter cycle. They found that large-scale polarity reversals occur with the longer cycle only, and if V889 Her behaves in the same way, this might explain why we have observed no polarity reversals here for V889 Her in phase with its 3–4 yr fluctuations. The short-term magnetic modulations may be a consequence of a near-surface dynamo. MHD simulations by Brun et al. (2022) with a near-surface dynamo for rapidly rotating stars produced short cycles (~ 1 yr), although these are marked by magnetic polarity reversals, with possible quasi-biennial oscillations.

It is clear from Fig. 4 that the magnetic field of V889 Her can also evolve much more rapidly compared to the 3–4 yr fluctuations, and that the apparent solar-like variability does not strictly hold across all of our observations. In 2019 June, the large-scale dipole of V889 Her crosses over the equator, but still does not fully reverse. The 2019 July 10–19 and 2019 July 20–29 observations seemingly capture the field evolution directly after an attempted reversal, and the magnetic field evolves rapidly during this time. Between 2019 June and 2019 July 10–19, the dipolar axis moves from the equator to 74° latitude, and the field strength drops as its structure becomes more simple. ~ 10 d later, in 2019 July 20–29, the magnetic field has

a similar complex structure to 2019 June and has an even stronger field strength, whereas the dipole latitude remains relatively high. This rapid, non-solar like evolution of the magnetic field could be similar to the chaotic field evolution observed for ϵ Eri during its short activity cycle. Metcalfe et al. (2013) and Petit et al. (2021) have also noted that ϵ Eridani potentially alternates between chaotic and cyclic variability. We speculate that the short-term evolution of the magnetic field in these young stars could potentially reflect the phase of the observations in the longer activity cycle. In the work of Jeffers et al. (2022), ϵ Eri is approaching a possible grand minimum in activity when its magnetic field is observed to vary chaotically. In our observations of V889 Her, the short-term variability resembles the solar cycle as the star approaches a grand maximum in activity around 2017 (Willamo et al. 2019b), inferred from the photometry in Fig. 5, and the field evolution is seemingly more chaotic afterwards.

The relationship between spot coverage and the large-scale magnetic field evolution is not entirely clear from our surface brightness and magnetic field maps. Both the spot-only and brightness + spot models suggest that the spot fraction reaches a local minimum in 2008 May, coinciding with minima in the magnetic field strength both from ZDI and the B_l, as well as a minimum in the chromospheric S-index. After 2008 May the spot evolution indicated by the spot-only and brightness + spot models are not consistent, and we cannot be sure which model is the most reliable. Based on the bright+spot models, a single spot cycle in V889 Her would seem to span two large-scale dipole reversal attempts in 2007 November and 2010 August, contrary to the solar case. Given that the photometric brightness varies much more rapidly than this, it is possible that the long spot cycle inferred by our DI results is an effect of infrequent sampling. The presence of both a long-lived polar spot and short-lived low-latitude features in V889 Her also makes deciphering patterns in mean spot coverage and photometric brightness difficult. Willamo et al. (2019b) compared spot occupancy to the same (unsmoothed) photometric data we show here. Their spot occupancy data showed rapid variability ($\sim$2–4 yr between local maxima) that would seem to correspond well with the magnetic field and photometric fluctuations shown by our results. For example, their spot filling factors peak between 2009 Sept and 2012 Aug., which is loosely consistent with peaks in the magnetic field strength, complexity and chromospheric activity shown by our observations. The peak amplitude of long-term photometric variations in Fig. 5 is $\sim$0.09 mag across the epochs of our DI observations, which corresponds to brightness variations of $\sim$ 9 per cent. The spot coverage from DI is, as expected, lower than the variability from photometry but is of a similar order.

4.4 Differential rotation

We measured a high level of differential rotation from several of our magnetic field maps, as shown in Fig. 2. For epochs with results not shown in Fig. 2, which have poorer phase coverage and sampling frequency, the χ^2 minimization tests either did not converge to a clear minimum, or we measured zero rotational shear. We consider these to be less reliable measurements. Modelling by Brown et al. (2011) suggested that differential rotation would change throughout a magnetic cycle due to dynamo waves, and observations of some cool stars support this (Petit, Donati & Collier Cameron 2004a), but it is not clear from our data if the evolution of the differential rotation parameters for V889 Her follow any trend with respect to the magnetic fluctuations. Like Marsden et al. (2007) did for IM Peg, we take the apparent epoch-to-epoch variations in the rotational shear of V889 Her, and the fact that the 1-σ uncertainty regions from different epochs overlap, as an indication that the uncertainty of our measurement is larger than suggested by individual epochs.
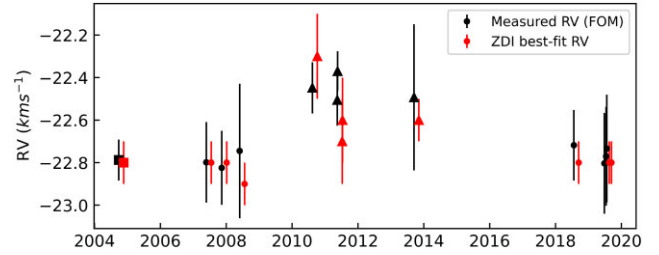
Figure 6. Comparison of the observed mean RV (black) for each DI epoch to the line-centre RV adopted to optimize the DI model fit (red, taken from Table B1). Squares, circles, and triangles indicate data from UCLES, NARVAL, and HARPS, respectively. The bars for the measured RVs show the standard deviation of the individual observations, and for the modelled line-centre RVs, the bars represent the uncertainties in the best-fitting line-centre RVs. The data in red have been shifted to the right for clarity.
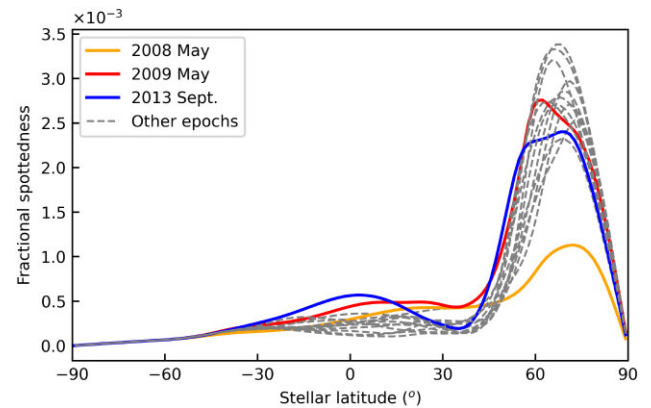
Figure 7. Fractional spot coverage versus stellar latitude for all of our DI maps. For epochs addressed in Section 5.1, the data are coloured, and the rest of the epochs are shown as dashed grey lines.

5 THE SEARCH FOR EXOPLANETS ORBITING V889 HER

5.1 RV variations on both short and long time-scales

The RV as measured from the Stokes *I* LSD observations shows both short-term fluctuations that relate to the rotation of magnetic surface features in and out of view, and also longer-term RV variability, the nature of which is unclear.

In Fig. 6, we show the mean and standard deviation of the observed RVs from Fig. 4 for each of our DI epochs (black markers). The standard deviation of the short-term RV variations is the greatest in 2013 September. This is also when the fractional spottedness at the equator is the greatest, according to Fig. 7 which shows the variation in fractional spottedness with stellar latitude for each of our DI models. The fractional spottedness was calculated in the same way as the fractional magnetic field strength, using equation (8), but with the average field strength at a latitude θ ($B(\theta)$) replaced by the average spot occupancy. Fig. 7 also shows high spot fractions at the mid-to-low latitudes in 2008 May and 2009 May, and the RVs in Fig. 6 show large standard deviations for these epochs. These data suggest that the amplitude of rotational RV modulations in V889 Her is most impacted by low-latitude surface features.

The short-term RV oscillations are not about a consistent RV, but rather a slightly varying RV across our observational epochs. This is consistent with the long-term RV variations observed over several months to years by Huber et al. (2009). For comparison against the
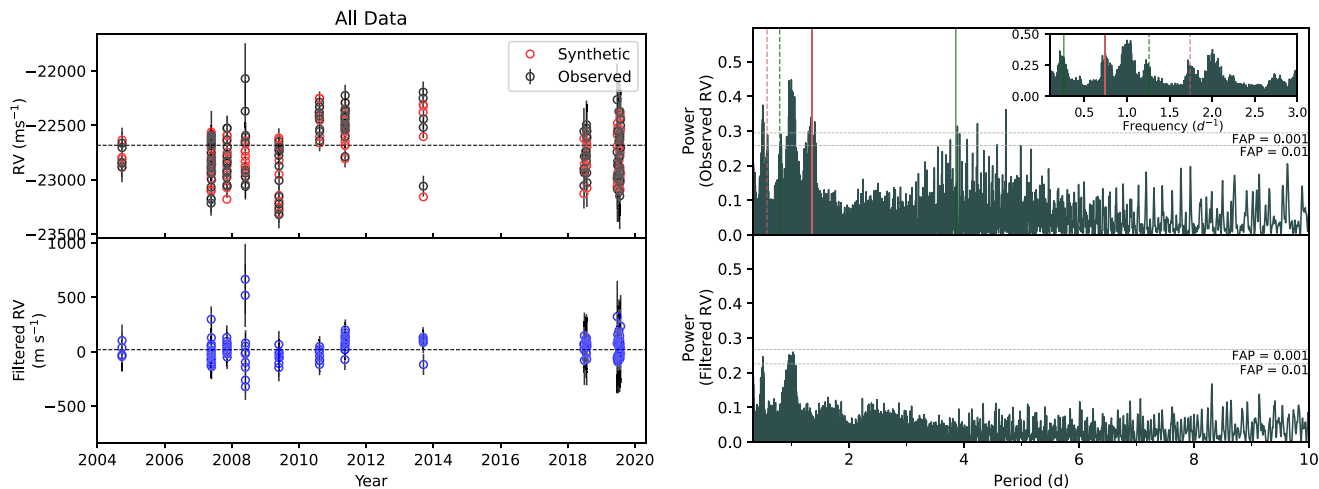
Figure 8. Left: Observed (black) and synthetic (red) RVs of V889 Her for combined data from all DI epochs (top) and residual RVs calculated by subtracting the synthetic from the observed RVs (bottom). Right: Power spectra for the observed (top) and residual (bottom) RVs, computed using the GLS periodogram. The solid red vertical line indicates the stellar rotational signal, and the solid green line indicates its alias at a frequency of $1 - \frac{1}{P_{rot}}$. Aliases of both of these signals repeat at frequency intervals of $1\,\mathrm{d}^{-1}$ and are indicated by the dashed red and green lines. Inset, we also include the power spectrum of the observed RVs in the frequency domain, where the aliasing of the rotational signal is more clear. The horizontal dashed grey lines indicate the periodogram power levels that correspond to a 0.1 per cent and 1 per cent FAP.

observed RV in Fig. 6, we also show in red the line-centre RV that optimized the DI model fit for each of the epochs. The apparent line-centre RV variations in Fig. 6 are not sufficiently larger than their uncertainties for us to believe they are true RV fluctuations, nor are the data adequate to carry out a period search, but we have adopted the fluctuating RVs to optimize the DI and ZDI model fits. In 2011 May 17–19, the offset between the observed and the best-fitting line-centre RV is the most significant, and this is also when the spot occupancy is the greatest in Fig. 4. Apart from this, there is no clear relationship between the two data sets in Fig. 6, and it is not clear if the long-term RV shifts can be explained by the magnetic activity evolution of V889 Her are indicative of a long-period companion, or a combination of the two. The HARPS data all show mean measured RVs that are higher compared to the AAT and NARVAL data, but we do not expect that the long-term RV fluctuations can be explained by an instrumental offset, because we corrected for the heliocentric velocity of the observatory toward the star and used telluric lines to reduce night-to-night shifts in the NARVAL and UCLES RVs, as discussed in Section 2.2.

5.2 DI activity modelling

Fig. 8 (top panel) shows the observed RVs and our synthetic, activity-induced RVs from DI, for a combination of data from all DI epochs. The 'filtered' RVs are shown in the bottom panel of Fig. 8, which are the residual values after subtracting the synthetic RVs from the observed RVs. DI filtering results in a 136 m s^{-1} improvement in the RV RMS (raw RVs have RMS ~ 250 m s^{-1} compared to $\sim$114 m s^{-1} for filtered RVs). Power spectra for the observed and residual RVs are also shown in Fig. 8, where significant frequencies in the data may correspond to a higher periodogram power. The power spectrum for the observed RVs is dominated by forests of peaks around the 1 d observing cadence and its aliases (0.5, 0.25 d, etc.). There are also forests of strong peaks around the rotation period (marked with a red line), an alias of the rotational signal at a frequency of $1 - \frac{1}{P_{rot}}$ d^{-1} (marked with a green line) which is related to the observing

cadence, as well as aliases of both of these signals that recur at frequency intervals of $\sim$1 d^{-1} (dashed red and green lines). The power spectrum for the filtered RVs shows residual peaks at periods of 1 and 0.5 d, related to the observing cadence. The results are similar for all other data sets we tested. The results for other selected data sets are provided as supplementary materials.

Although the power spectra in Fig. 8 prove we were able to remove the activity-related rotational RV signal and its aliases by subtracting the synthetic RVs, we were still unable to recover any significant periodicities in the residuals outside those related to the observing cadence, and this is an impact of the limited temporal coverage of our data. For V889 Her, longer periods of dense observations could improve exoplanet detection capabilities, but care will need to be taken when using the DI activity filtering technique because of the underlying long-term RV variability. We are not sure of the nature of the long-term RV shifts, but the varying line-centre RVs adopted for each DI epoch undoubtedly bias the DI activity filtering and thus the exoplanet search. The impact would likely be the greatest when searching for long-period companions, such as planets orbiting within the habitable zone.

5.3 GPR activity modelling

We also tested GPR to model the magnetic activity of V889 Her, using a quasi-periodic GP kernel which has been shown to be highly effective at reproducing rotationally modulated activity-induced RVs (e.g. Haywood et al. 2014; Angus et al. 2018; Heitzmann et al. 2021; Perger et al. 2021). However, our GPR models did not converge to a reasonable solution for any of our activity-only or activity + exoplanet tests, so here we explore the challenges of applying GPR to V889 Her as a test case for young solar analogues.

5.3.1 Issue 1: Different decay time-scales for polar and lower-latitude spots

A key issue was constraining the hyper-parameter θ_2, which relates to the time-scale for active region growth and decay. When we applied

GPR to single epochs of data θ_2 did not converge to a realistic solution (Fig. D1). Potentially, the RV signal related to the long-lived polar spot obfuscates the signal from lower-latitude features, which we would expect to decay rapidly over ~ 3 to 15 d based on our brightness and magnetic maps, and the *TESS* light curve in Fig. A1. The polar-spot evolves on a time-scale much longer than a single epoch of data and Nicholson & Aigrain (2022) found that θ_2 breaks down when this occurs.

When combining data from multiple epochs the GP could fit to either short (several days) or long (several thousand days) spot decay time-scales depending on the prior used for θ_2 (see Fig. D2). There was not a significant difference in the log of the Bayesian evidence between these models, so the preferred model is unclear.

5.3.2 Issue 2: Strong differential rotation

When fitting to multiple epochs of data the posterior distribution of the rotation period, θ_3, seemed to be correlated with the decay time-scale. A slightly longer rotation period was associated with a longer spot decay time-scale (likely related to the polar spot), and vice versa. When we fitted the GP to the entire ~ 15 yr of data, θ_3 even showed a bimodal distribution (Fig. D3). This is probably related to the significant differential rotation exhibited by V889 Her, which means that the RV modulations caused by spots at different latitudes will have different periods.

5.3.3 Issue 3: Insufficient temporal coverage of data

Given the above two issues, the temporal coverage of our legacy data is insufficient to model the activity-induced RVs for V889 Her using GPR. Our data are not overall very different from that used by Heitzmann et al. (2021; 23 UCLES spectra covering 11 d or 4.68 stellar rotations), but they found that a quasi-periodic GP could satisfactorily reproduce the activity-induced RVs of HD 141943 for a single observational epoch. Their target has a rotation period roughly double that of V889 Her, at 2.198 ± 0.002 d and lower differential rotation rate at $d\Omega = 0.1331^{+0.0095}_{-0.0094}$ rad d^{-1} compared to 0.319 rad d^{-1} for V889 Her (although they measured DR from the Stokes *I* profiles while we used Stokes *V* profiles). Their reconstructed DI images indicate a polar spot that appears to be somewhat smaller compared to the polar spot on V889 Her, and they recovered low-latitude features with a similar strength to the polar spot and much larger area coverage compared to in V889 Her, for which the low-latitude features are weak and small relative to the polar spot. The strength of the lower latitude features relative to the polar spot, and the low differential rotation rate in HD 141943, may explain why the GP converges easily for the moderately active star in Heitzmann et al. (2021).

Another issue in modelling magnetic activity for V889 Her is the underlying long-term RV variations and the fact that our observations with different instruments have no temporal overlap. The mean RV from HARPS is ~ 300 m s^{-1} higher compared to the AAT and NARVAL RVs, differences that the GP can easily account for with large instrumental offsets, but this dilutes the contributions of activity and any exoplanets. Given that we corrected for the heliocentric velocity of the observatory towards the star and used telluric lines to reduce night-to-night shifts in the NARVAL and UCLES RVs, we do not expect such large RV differences between the data sets to be entirely instrumental.

It is clear from our results that DI is more suitable compared to GPR for modelling the magnetic activity of V889 Her using our current data set. DI has more flexibility to model complex magnetic activity, compared to our quasi-periodic GP model. However, DI

cannot resolve small scale magnetic structures, which Jeffers et al. (2014) and Lisogorskyi et al. (2020) showed can prevent the detection of up to 20 $M_\oplus$ planets in temperate zones around Sun-like stars. Therefore, it is important that we improve data-driven techniques such as GPR to model the magnetic activity of young Suns.

5.3.4 Recommendations for modelling extreme magnetic activity with GPR

Although Perger et al. (2021) found that a quasi-periodic GP can fit well individually to solar-like low-latitude spot configurations, or polar spots, our results suggest that the quasi-periodic GP may not be able to constrain the activity evolution for a combination of the two when significant differential rotation is present, at least when using legacy data with large gaps. Future observing plans should focus on obtaining long time-series of continuous high-cadence observations, ideally with nightly observations spanning a few months as is carried out with the RedDots exoplanet search program (Jeffers et al. 2020). Exploration of alternative GP covariance kernels and simultaneous modelling of RVs and activity indicators are also recommended. We performed some preliminary tests combining a quasi-periodic and stable periodic GP component (Kossakowski et al. 2022) to model contributions of the low-latitude and polar features, respectively, to the activity-induced RVs, but the GP did not converge for our tests.

5.4 Exoplanet detection limits with DI

We used V889 Her to estimate the detection limits for HJs orbiting extremely active stars when using existing legacy data and filtering activity jitter using DI. We injected synthetic planetary RV shifts into our data, re-computed our DI models and then searched the DI-subtracted RVs for the injected planetary signals. The planet-induced RV shifts were calculated using equation (6), assuming a circular orbit, and the shifts were applied to the observed LSD line profiles. We limited our tests to planets with orbital periods of 3–7 d (orbiting at ~ 0.04–0.07 au), and masses of 1–2 M_{Jup}.

Given our ~ 15 yr data set, we estimate that we could, in principle, detect Jupiter-mass planets with orbital periods of 3 d. Fig. 9 (top) shows the power spectrum for the entire series of RVs with the injected 3 d, $1 M_{Jup}$ planetary signal, and the power spectrum of the DI-subtracted RVs. The DI-subtracted RVs show a 3 d peak that is significant with respect to the 0.1 per cent FAP level.

At orbital periods of 4–5 d, the planetary signal is buried under a forest of peaks with periods around $1/(1 + f_{rot})$, which are aliases of the stellar rotational signal. The rotational signal and its aliases are removed by DI such that 2 M_{Jup} planets at these orbital periods would be detectable with a FAP < 1 per cent, as shown in the second panel of Fig. 9. 2 M_{Jup} planets with orbital periods of 6–7 d are detectable in the DI-subtracted RVs with a FAP < 1 per cent. However, for these longer orbital periods, there are several strong signals shown in the DI-subtracted RVs and selecting the correct peak is non-trivial. This issue arises as the orbital period becomes similar to the length of most our individual epochs of observations.

6 CONCLUSIONS

In this study, we used previously published and new spectropolari-metric data spanning the years 2004–2019, with archival photometry taken between 1994 and 2018, to investigate the variability of the magnetic field, surface activity and RV of the young solar analogue V889 Her. We also tested the techniques of Doppler Imaging (DI) and Gaussian Process Regression (GPR) to filter activity-induced RV variations and search the residual RVs for exoplanets.
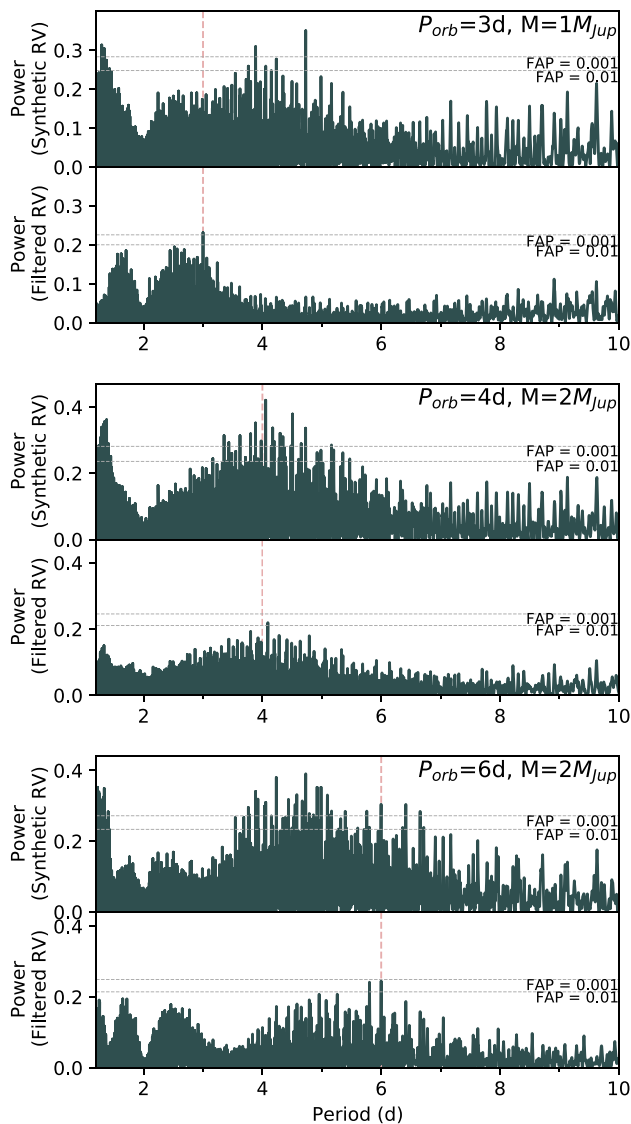
Figure 9. Power spectra for synthetic and DI-subtracted RVs (all epochs combined), where the RVs include a synthetic planetary signal with a period and planetary mass as indicated. The dashed red vertical line in each panel indicates the period of the injected planet. The horizontal dashed grey lines indicate the periodogram power levels that correspond to a 0.1 per cent and 1 per cent FAP, which were computed as in Section 5.2. We have excluded periods ≤ 1.2 d, for which the power spectrum is dominated by peaks related to the observing cadence and its aliases.

Our magnetic maps indicate possible quasi-periodic magnetic field fluctuations with a potential period of 3–4 yr. The magnetic field evolution during this period loosely resembles the solar magnetic cycle; the field is simple and dominantly poloidal during magnetic and chromospheric activity minima and is complex and dominantly toroidal during a magnetic and chromospheric activity maxima. Smoothed photometric data show a 7–9 yr brightness cycle and short-term brightness oscillations with a period of 1–1.5 yr, roughly half the length of the magnetic field oscillation we observed. Contrary to the solar case, no large-scale polarity reversals were observed for V889 Her, but several attempts at polarity reversals were observed. Long-term monitoring will be required to determine if the star

undergoes large-scale magnetic polarity reversals and if it truly switches between solar-like and non-solar-like behaviour.

Our surface brightness maps confirmed the presence of both a large, long-lived polar spot and multiple smaller short-lived spots at low- to mid-latitudes. The observed stellar RV showed significant rotational modulation, its amplitude tied to the spot coverage at low latitudes. The RVs also showed underlying long-term fluctuations of unconfirmed origin.

We were unable to reliably fit a quasi-periodic GP model to the stellar activity-induced RV variations due to three main challenges:

(i) There are competing RV signals from the long-lived and temporally varying polar spot and rapidly evolving low-latitude features;

(ii) There is significant differential rotation; and

(iii) The temporal coverage of our legacy data is insufficient.

To help overcome these challenges, we recommend that alternative GP kernels be tested and high-cadence observations of V889 Her (or similar stars) be carried out for as long as possible, ideally with nightly observations spanning a few months as is carried out with the RedDots exoplanet search program (Jeffers et al. 2020).

When using existing legacy data, the DI technique can be a useful tool for modelling the activity-induced RV variability of active young Suns, with the flexibility to model complex surface spot distributions. Using the DI method we were able to remove the activity-related rotational RV signal and its aliases. Given our ∼ 15 yr set of RV observations we estimate that we could, in principle, detect the presence of a 1 M_{Jup} planet with an orbital period of ∼ 3 d and, with less certainty, 2 M_{Jup} planets with orbital periods between 3 and 7 d.

DATA AVAILABILITY

Spectropolarimetric data are available via PolarBase (http://polarbase.irap.omp.eu/), the ESO archive (http://archive.eso.org/cms.html), and AAT archive (https://archives.datacentral.org.au/). *TESS* data can be found at the Barbara A. Mikulski Archive for Space Telescopes (MAST, https://mast.stsci.edu/), and the differential V-band photometry is available on VIZIER (Willamo et al. 2019a).

REFERENCES

Angus R., Morton T., Aigrain S., Foreman-Mackey D., Rajpaul V., 2018, MNRAS, 474, 2094

Astropy Collaboration, 2013, A&A, 558, A33

Aurière M., 2003, in Arnaud J., Meunier N., eds, EAS Publications Ser. Vol. 9. EAS, Toulouse, France, p. 105

Barnes S. A., 2007, ApJ, 669, 1167

Barnes J. R., Jeffers S. V., Jones H. R. A., 2011, MNRAS, 412, 1599

Barnes J. R. et al., 2017, MNRAS, 466, 1733

Baudrand J., Bohm T., 1992, A&A, 259, 711

Boro Saikia S. et al., 2016, A&A, 594, A29

Boro Saikia S. et al., 2018, A&A, 620, L11

Boro Saikia S. et al., 2022, A&A, 658, A16

Brown S. F., Donati J. F., Rees D. E., Semel M., 1991, A&A, 250, 463

Brown B. P., Miesch M. S., Browning M. K., Brun A. S., Toomre J., 2011, ApJ, 731, 69

Brown E. L. et al., 2021, MNRAS, 501, 3981

Brun A. S., Strugarek A., Noraz Q., Perri B., Varela J., Augustson K., Charbonneau P., Toomre J., 2022, ApJ, 926, 21

Buchner J. et al., 2014, A&A, 564, A125

Collier Cameron A., 2001, in Boffin H. M. J., Steeghs D., Cuypers J., eds, Astrotomography, Indirect Imaging Methods in Observational Astronomy, Vol. 573, Lecture Notes in Physics. Springer, Berlin, Heidelberg, p. 183

DeRosa M. L., Brun A. S., Hoeksema J. T., 2012, ApJ, 757, 96

Donati J. F., Brown S. F., 1997, A&A, 326, 1135

Donati J. F., Semel M., Carter B. D., Rees D. E., Collier Cameron A., 1997, MNRAS, 291, 658

Donati J. F., Catala C., Wade G. A., Gallou G., Delaigue G., Rabou P., 1999, A&AS, 134, 149

Donati J. F. et al., 2003, MNRAS, 345, 1145

Donati J.-F. et al., 2006, MNRAS, 370, 629

Donati J. F. et al., 2008, MNRAS, 385, 1179

Donati J. F. et al., 2014, MNRAS, 444, 3220

Fares R. et al., 2009, MNRAS, 398, 1383

Feroz F., Hobson M. P., Bridges M., 2009, MNRAS, 398, 1601

Folsom C. P. et al., 2018, MNRAS, 474, 4956

Foreman-Mackey D., 2016, J. Open Source Softw., 1, 24

Frasca A., Biazzo K., Kővári Z., Marilli E., Çakırlı Ö., 2010, A&A, 518, A48

Gomes da Silva J. et al., 2021, A&A, 646, A27

Gray D. F., 2005, The Observation and Analysis of Stellar Photospheres, 3rd edn. Cambridge Univ. Press, Cambridge

Harris C. R. et al., 2020, Nature, 585, 357

Haywood R. D. et al., 2014, MNRAS, 443, 2517

Heitzmann A. et al., 2021, MNRAS, 505, 4989

Huber K. F., Wolter U., Czesla S., Schmitt J. H. M. M., Esposito M., Ilyin I., González-Pérez J. N., 2009, A&A, 501, 715

Humlíček J., 1982, J. Quant. Spec. Radiat. Transf., 27, 437

Hunter J. D., 2007, Comput. Sci. Eng., 9, 90

Järvinen S. P., Korhonen H., Berdyugina S. V., Ilyin I., Strassmeier K. G., Weber M., Savanov I., Tuominen I., 2008, A&A, 488, 1047

Jeffers S. V., Donati J. F., 2008, MNRAS, 390, 635

Jeffers S. V., Donati J. F., Alecian E., Marsden S. C., 2011, MNRAS, 411, 1301

Jeffers S. V., Barnes J. R., Jones H. R. A., Reiners A., Pinfield D. J., Marsden S. C., 2014, MNRAS, 438, 2717

Jeffers S. V. et al., 2018, MNRAS, 479, 5266

Jeffers S. V. et al., 2020, Science, 368, 1477

Jeffers S. V. et al., 2022, A&A, 661, A152

Kossakowski D. et al., 2022, A&A, 666, A143

Lehmann L. T., Hussain G. A. J., Jardine M. M., Mackay D. H., Vidotto A. A., 2019, MNRAS, 483, 5246

Lehtinen J., Jetsu L., Hackman T., Kajatkari P., Henry G. W., 2016, A&A, 588, A38

Lehtinen J. J. et al., 2022, A&A, 660, A141

Lienhard F., Mortier A., Buchhave L., Collier Cameron A., López-Morales M., Sozzetti A., Watson C. A., Cosentino R., 2022, MNRAS, 513, 5328

Lisogorskyi M. et al., 2020, MNRAS, 497, 4009

Lomb N. R., 1976, Ap&SS, 39, 447

Luck R. E., 2018, AJ, 155, 111

Marsden S. C., Donati J. F., Semel M., Petit P., Carter B. D., 2006, MNRAS, 370, 468

Marsden S. C., Berdyugina S. V., Donati J. F., Eaton J. A., Williamson M. H., 2007, Astron. Nachr., 328, 1047

Marsden S. C. et al., 2014, MNRAS, 444, 3517

Mengel M. W., Fares R., Marsden S. C., Carter B. D., Jeffers S. V., Petit P., Donati J.-F., Folsom C. P., 2016, MNRAS, 459, 4325

Metcalfe T. S. et al., 2013, ApJ, 763, L26

Meunier N., Desort M., Lagrange A. M., 2010, A&A, 512, A39

Montes D., López-Santiago J., Gálvez M. C., Fernández-Figueroa M. J., De Castro E., Cornide M., 2001, MNRAS, 328, 45

Moutou C. et al., 2007, A&A, 473, 651

Nava C., López-Morales M., Haywood R. D., Giles H. A. C., 2020, AJ, 159, 23

Nicholson B. A., Aigrain S., 2022, MNRAS, 515, 5251

Oláh K., Kővári Z., Petrovay K., Soon W., Baliunas S., Kolláth Z., Vida K., 2016, A&A, 590, A133

Perger M., Anglada-Escudé G., Ribas I., Rosich A., Herrero E., Morales J. C., 2021, A&A, 645, A58

Petit P., Donati J. F., Collier Cameron A., 2004a, Astron. Nachr., 325, 221

Petit P. et al., 2004b, MNRAS, 348, 1175

Petit P. et al., 2021, A&A, 648, A55

Radick R. R., Lockwood G. W., Baliunas S. L., 1990, Science, 247, 39

Scargle J. D., 1982, ApJ, 263, 835

See V. et al., 2016, MNRAS, 462, 4442

Semel M., Donati J. F., Rees D. E., 1993, A&A, 278, 231

Şenavcı H. V., Kılıçoğlu T., Işık E., Hussain G. A. J., Montes D., Bahar E., Solanki S. K., 2021, MNRAS, 502, 3343

Snik F. et al., 2011, in Kuhn J. R., Harrington D. M., Lin H., Berdyugina S. V., Trujillo-Bueno J., Keil S. L., Rimmele T., eds, ASP Conf. Ser. Vol. 437, Solar Polarization 6. Astron. Soc. Pac., San Francisco, p. 237

Solanki S. K., Unruh Y. C., 2004, MNRAS, 348, 307

Strassmeier K. G., Pichler T., Weber M., Granzer T., 2003, A&A, 411, 595

Trifonov T., Tal-Or L., Zechmeister M., Kaminski A., Zucker S., Mazeh T., 2020, A&A, 636, A74

Trotta R., 2008, Contemp. Phys., 49, 71

Virtanen P. et al., 2020, Nature Methods, 17, 261

Wade G. A., Donati J. F., Landstreet J. D., Shorlin S. L. S., 2000a, MNRAS, 313, 823

Wade G. A., Donati J. F., Landstreet J. D., Shorlin S. L. S., 2000b, MNRAS, 313, 851

Willamo T. et al., 2019a, VizieR Online Data Catalog, J/A+A/622/A170

Willamo T. et al., 2019b, A&A, 622, A170

Willamo T., Hackman T., Lehtinen J. J., Korpi-Lagg M., Kochukhov O., 2022a, Open J. Astrophys., 5, 10

Willamo T., Lehtinen J. J., Hackman T., Käpylä M. J., Kochukhov O., Jeffers S. V., Korhonen H., Marsden S. C., 2022b, A&A, 659, A71

Wilson O. C., 1978, ApJ, 226, 379

Zechmeister M., Kürster M., 2009, A&A, 496, 577

Zechmeister M., Kürster M., Endl M., 2009, A&A, 505, 859

SUPPORTING INFORMATION

Supplementary data are available at *MNRAS* online.

**EBrown_V889Her_resub3_supplementary.pdf**

Please note: Oxford University Press is not responsible for the content or functionality of any supporting materials supplied by the authors. Any queries (other than missing material) should be directed to the corresponding author for the article.

APPENDIX A: TESS PHOTOMETRY

Fig. A1 shows TESS photometry from sectors 26, 40, and 53, where V889 Her was observed in 2-min integrations. Power spectra derived using the GLS periodogram (Zechmeister & Kürster 2009) are also shown for each data set.

APPENDIX B: ZDI RESULTS

Table B1 summarizes the ZDI model outputs, and Figs B1, B2 and B3 show the brightness and magnetic field maps for each of our 14 observational epochs. Model fits corresponding to each set of maps are shown in Figs 1–4 of the supplementary materials.
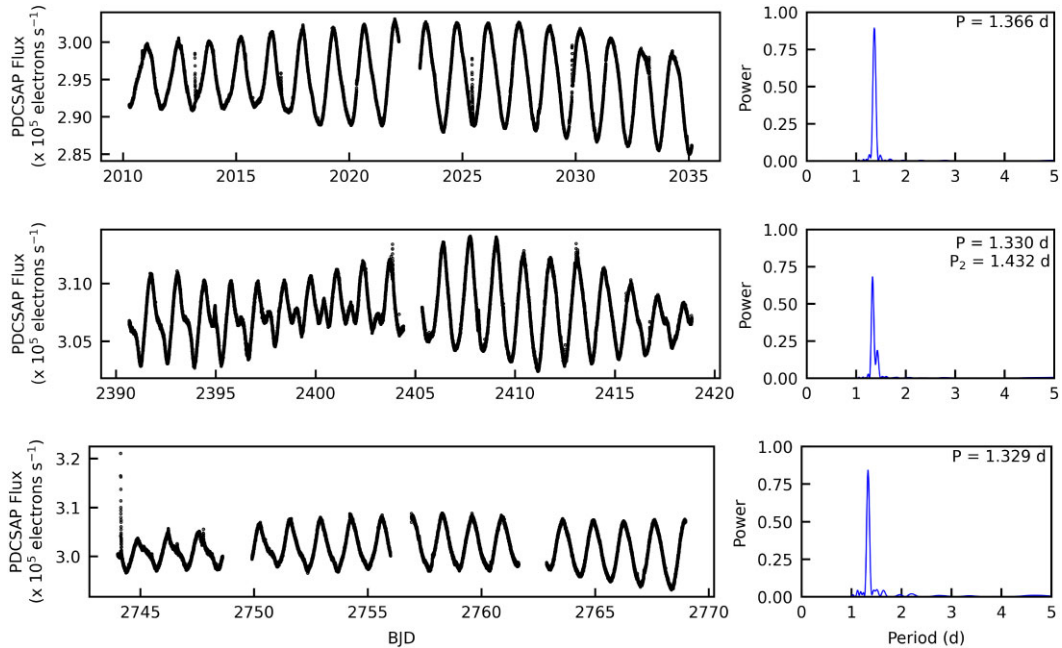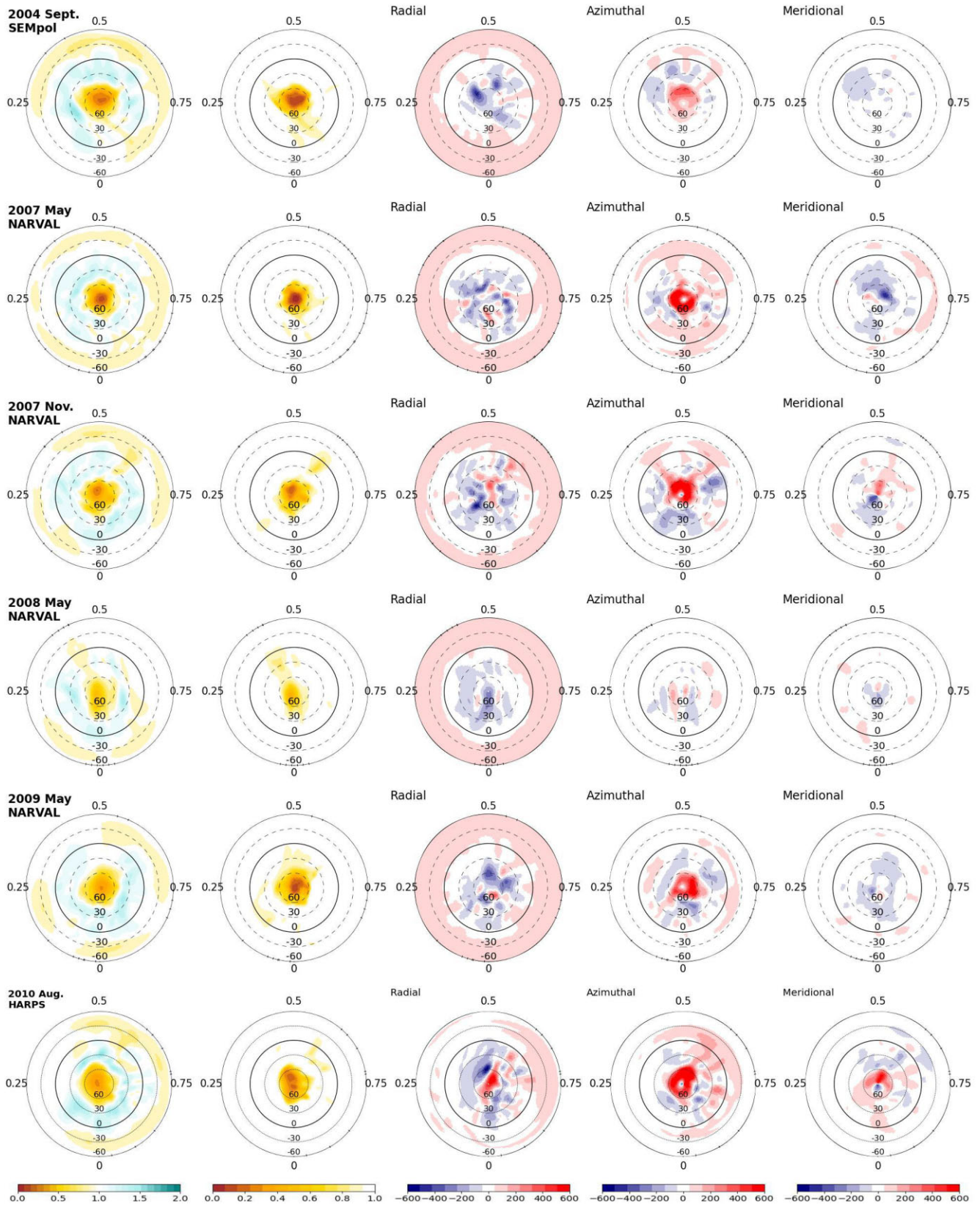

Figure A1. *TESS* Pre-search Data Conditioned Single Aperture Photometry (PDCSAP) observations of V889 Her from sectors 26 (top), 40 (middle), and 53 (bottom). The data show clear rotational modulation related to brightness contrasts on the stellar surface. Occasional vertical lines in the flux are indicative of flares. Power spectra derived using the GLS periodogram are also shown on the right of each data set, and the period of the brightness modulation is indicated as P. For sector 40 (middle), P_2 is the period related to the secondary power spectrum peak.

Table B1. Surface brightness and large-scale magnetic field properties for 2004 September through to 2019 July. Columns (left to right) indicate the best-fitting RV for each epoch, the mean percentage of the stellar surface covered by dark spots for a spot-only model ([0:1]), the mean spot coverage (relative to a quiet photosphere with 100 per cent brightness [0:2]) for a bright+spot model, and mean surface brightness (relative to a quiet photosphere ([0:1]), the fraction of the total magnetic energy stored in the poloidal component, the percentages of poloidal and toroidal energy stored in dipolar ($l = 1$), quadrupolar ($l = 2$), and octopolar modes ($l = 3$), the percentages of the total, poloidal, and toroidal field energies stored in axisymmetric modes and the strength and location of the negative pole of the radial component of the large-scale dipole. The upper and lower values shown for each measured parameter represent their sensitivity to variations in the $P_{\rm rot}$ ($^{+0.012}_{-0.011}$ d), $d\Omega$ (± 0.114 rad d^{-1}), $v \sin i$ (± 0.5 km s^{-1}), and RV (± 0.1 km s^{-1}). The magnetic field parameters reported in Table B1 were provided by the authors of Jeffers & Donati (2008).
* The 2005 May data originally published in Jeffers & Donati (2008) was not reanalysed here.

Map	RV ($km\,s^{-1}$)	Mean spot (%, spot-only)	Mean spot (%, S+B)	Mean bright (%, S+B)	$B_{\rm mean}$ (G)	$B_{\rm max}$ (G)	Poloidal % tot	$l=1$	$l=2$	$l=3$	Toroidal $l=1$	$l=2$	$l=3$	Axisym % tot	% Pol	% Tor	Dipole radial -ve B (G)	Lat.
2004 September	-22.8 ± 0.1	$6.8^{+1.7}_{-0.6}$	$10.5^{+2.6}_{-0.7}$	$97.2^{+0.1}_{-0.6}$	95^{+7}_{-3}	549^{+16}_{-8}	62^{+2}_{-1}	37^{+0}_{-1}	8^{+0}_{-0}	9^{+1}_{-1}	2^{+1}_{-0}	8^{+0}_{-1}	33^{+1}_{-1}	52^{+1}_{-2}	38^{+1}_{-2}	75^{+1}_{-2}	-97^{+4}_{-5}	70^{+0}_{-0}
2005 May*	-22.9 ± 0.1	-	-	-	113	462	47	45	3	10	1	2	9	47	36	57	-105	49
2007 May	-22.8 ± 0.1	$5.4^{+2.9}_{-0.0}$	$8.7^{+4.6}_{-0.0}$	$97.4^{+0.1}_{-0.1}$	141^{+22}_{-0}	912^{+120}_{-0}	34^{+3}_{-1}	20^{+0}_{-8}	17^{+6}_{-0}	5^{+1}_{-2}	8^{+1}_{-0}	6^{+0}_{-0}	15^{+1}_{-2}	66^{+0}_{-2}	35^{+1}_{-4}	81^{+0}_{-1}	-84^{+14}_{-0}	76^{+0}_{-6}
2007 November	-22.8 ± 0.1	$5.5^{+2.2}_{-0.4}$	$9.2^{+5.5}_{-0.0}$	$97.7^{+0.1}_{-0.0}$	136^{+29}_{-5}	813^{+248}_{-0}	45^{+0}_{-4}	24^{+2}_{-6}	8^{+1}_{-1}	11^{+1}_{-0}	2^{+0}_{-0}	6^{+0}_{-0}	23^{+1}_{-1}	40^{+0}_{-1}	13^{+2}_{-0}	63^{+1}_{-1}	-86^{+0}_{-1}	50^{+0}_{-3}
2008 May	-22.9 ± 0.1	$3.6^{+0.9}_{-0.0}$	$5.8^{+1.1}_{-0.0}$	$98.5^{+0.0}_{-0.2}$	78^{+2}_{-0}	329^{+0}_{-0}	85^{+0}_{-1}	62^{+0}_{-2}	5^{+1}_{-0}	4^{+0}_{-0}	1^{+0}_{-0}	1^{+0}_{-0}	1^{+0}_{-0}	58^{+0}_{-2}	66^{+0}_{-2}	15^{+2}_{-1}	-110^{+1}_{-1}	70^{+0}_{-1}
2009 May	-22.9 ± 0.1	$7.2^{+2.3}_{-0.0}$	$8.8^{+2.3}_{-0.1}$	$97.8^{+0.0}_{-0.5}$	123^{+15}_{-8}	643^{+102}_{-15}	52^{+0}_{-0}	28^{+0}_{-2}	8^{+0}_{-0}	9^{+0}_{-0}	2^{+1}_{-0}	3^{+0}_{-0}	19^{+1}_{-1}	53^{+0}_{-1}	36^{+0}_{-1}	72^{+0}_{-1}	-107^{+6}_{-8}	90^{+0}_{-1}
2010 August	-22.3 ± 0.2	$6.9^{+2.8}_{-0.0}$	$10.5^{+2.2}_{-0.0}$	$97.3^{+0.0}_{-0.5}$	156^{+20}_{-5}	1239^{+71}_{-87}	47^{+3}_{-0}	9^{+3}_{-2}	12^{+1}_{-2}	15^{+0}_{-1}	10^{+2}_{-0}	3^{+1}_{-1}	18^{+1}_{-2}	54^{+4}_{-4}	32^{+2}_{-6}	73^{+1}_{-2}	-47^{+2}_{-17}	28^{+16}_{-14}
2011 May 14–16	-22.7 ± 0.2	$6.9^{+1.3}_{-0.0}$	$12.1^{+1.9}_{-0.0}$	$96.6^{+0.0}_{-0.5}$	158^{+16}_{-4}	938^{+78}_{-52}	64^{+1}_{-1}	31^{+4}_{-0}	25^{+4}_{-1}	10^{+1}_{-1}	6^{+0}_{-0}	9^{+0}_{-1}	21^{+1}_{-1}	60^{+2}_{-1}	59^{+3}_{-3}	64^{+1}_{-0}	-131^{+1}_{-0}	58^{+0}_{-4}
2011 May 17–19	-22.6 ± 0.2	$7.1^{+2.8}_{-0.0}$	$11.6^{+2.4}_{-0.0}$	$96.7^{+0.0}_{-0.6}$	158^{+22}_{-6}	840^{+106}_{-54}	69^{+0}_{-2}	28^{+3}_{-3}	22^{+5}_{-0}	11^{+1}_{-0}	9^{+1}_{-1}	6^{+0}_{-1}	19^{+1}_{-0}	54^{+3}_{-1}	51^{+3}_{-4}	62^{+3}_{-3}	-116^{+12}_{-5}	58^{+0}_{-6}
2013 September 11–15	-22.6 ± 0.1	$7.0^{+1.8}_{-0.1}$	$9.3^{+3.2}_{-0.7}$	$97.9^{+0.2}_{-0.2}$	102^{+1}_{-0}	530^{+0}_{-27}	69^{+2}_{-1}	25^{+1}_{-0}	14^{+2}_{-2}	12^{+2}_{-2}	31^{+3}_{-3}	22^{+1}_{-1}	16^{+3}_{-3}	22^{+3}_{-3}	5^{+1}_{-1}	60^{+2}_{-4}	-42^{+3}_{-4}	24^{+7}_{-3}
2018 June	-22.9 ± 0.1	$5.4^{+1.3}_{-0.3}$	$8.5^{+1.9}_{-1.1}$	$98.0^{+0.3}_{-0.5}$	87^{+4}_{-3}	357^{+10}_{-0}	51^{+7}_{-0}	26^{+4}_{-6}	5^{+2}_{-1}	17^{+3}_{-3}	4^{+2}_{-1}	4^{+1}_{-0}	44^{+4}_{-3}	54^{+1}_{-9}	24^{+3}_{-6}	84^{+0}_{-3}	-65^{+2}_{-3}	68^{+0}_{-3}
2018 July 17–28	-22.8 ± 0.1	$5.7^{+2.2}_{-0.6}$	$9.1^{+2.1}_{-0.9}$	$97.6^{+0.2}_{-0.6}$	134^{+15}_{-0}	703^{+0}_{-70}	47^{+4}_{-1}	22^{+2}_{-3}	6^{+0}_{-1}	13^{+5}_{-3}	4^{+2}_{-1}	4^{+0}_{-0}	32^{+2}_{-4}	46^{+0}_{-5}	10^{+1}_{-1}	78^{+0}_{-5}	-78^{+0}_{-8}	42^{+1}_{-4}
2019 June	-22.8 ± 0.1	$5.9^{+1.4}_{-0.5}$	$9.7^{+2.1}_{-0.9}$	$97.5^{+0.2}_{-0.6}$	149^{+30}_{-8}	1152^{+268}_{-81}	60^{+0}_{-2}	11^{+2}_{-0}	17^{+1}_{-0}	24^{+1}_{-2}	4^{+2}_{-1}	4^{+0}_{-0}	29^{+1}_{-0}	41^{+4}_{-8}	30^{+7}_{-8}	57^{+2}_{-2}	-69^{+0}_{-15}	-12^{+9}_{-22}
2019 July 10–19	-22.8 ± 0.1	$6.0^{+1.2}_{-0.6}$	$8.8^{+2.1}_{-0.8}$	$98.1^{+0.1}_{-0.5}$	124^{+12}_{-5}	438^{+63}_{-0}	69^{+4}_{-5}	27^{+1}_{-5}	14^{+0}_{-3}	11^{+1}_{-2}	9^{+2}_{-2}	4^{+3}_{-2}	29^{+2}_{-6}	45^{+2}_{-3}	36^{+2}_{-6}	64^{+9}_{-6}	-109^{+14}_{-10}	74^{+4}_{-6}
2019 July 20–29	-22.8 ± 0.1	$5.5^{+1.2}_{-0.4}$	$9.4^{+1.9}_{-0.9}$	$97.5^{+0.2}_{-0.4}$	165^{+32}_{-7}	1082^{+258}_{-19}	45^{+2}_{-1}	22^{+3}_{-5}	7^{+1}_{-0}	10^{+1}_{-0}	1^{+0}_{-0}	2^{+0}_{-0}	32^{+3}_{-3}	50^{+2}_{-2}	21^{+1}_{-1}	74^{+1}_{-2}	-115^{+1}_{-1}	62^{+0}_{-1}

Figure B1. Left to right: reconstructed brightness + spot, spot-only, radial field, azimuthal field, and meridional field maps for V889 Her, from 2004 September through to 2010 August. The maps are flattened polar projections, showing the visible pole at the centre and with latitudes extending down to -60°. Radial ticks indicate the phases of observations.
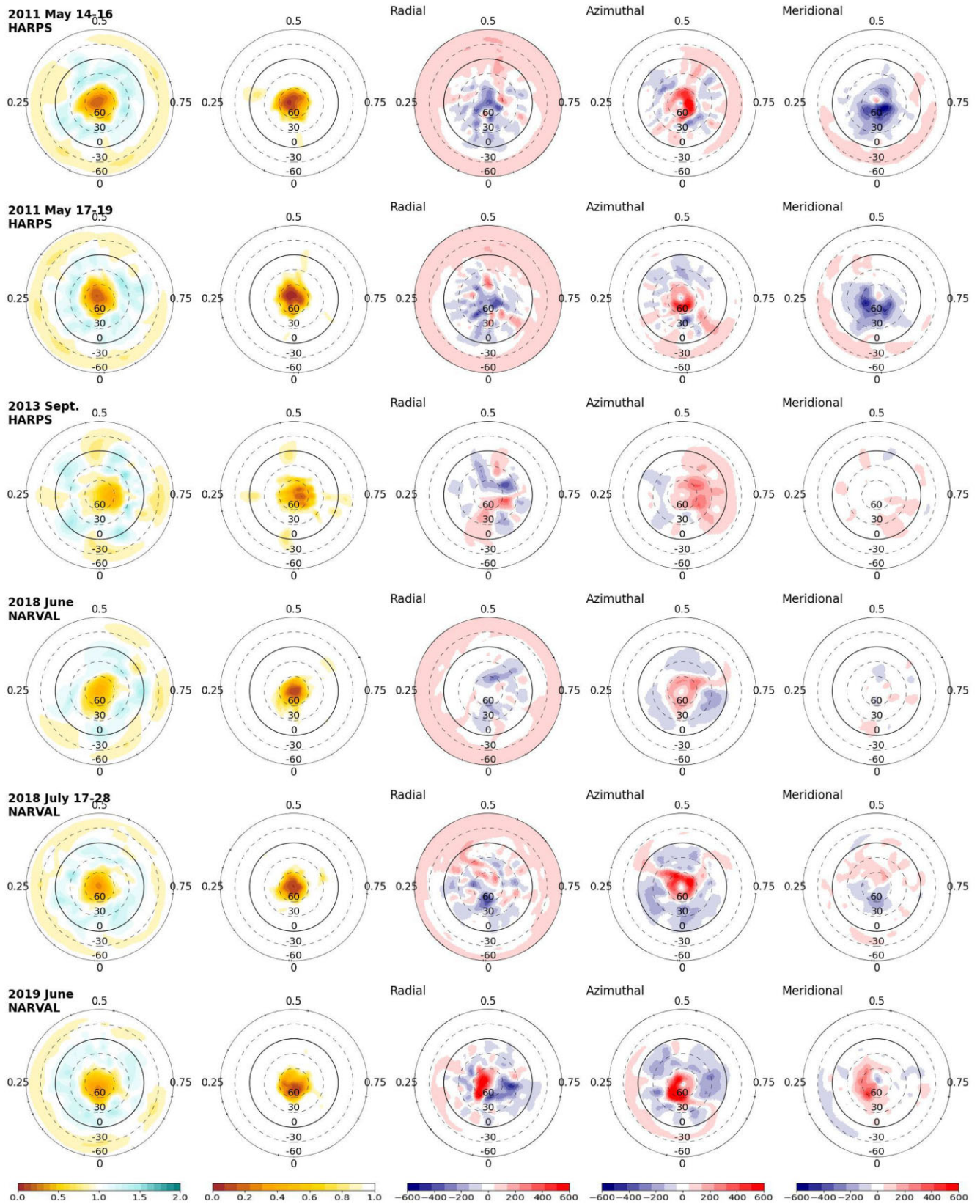
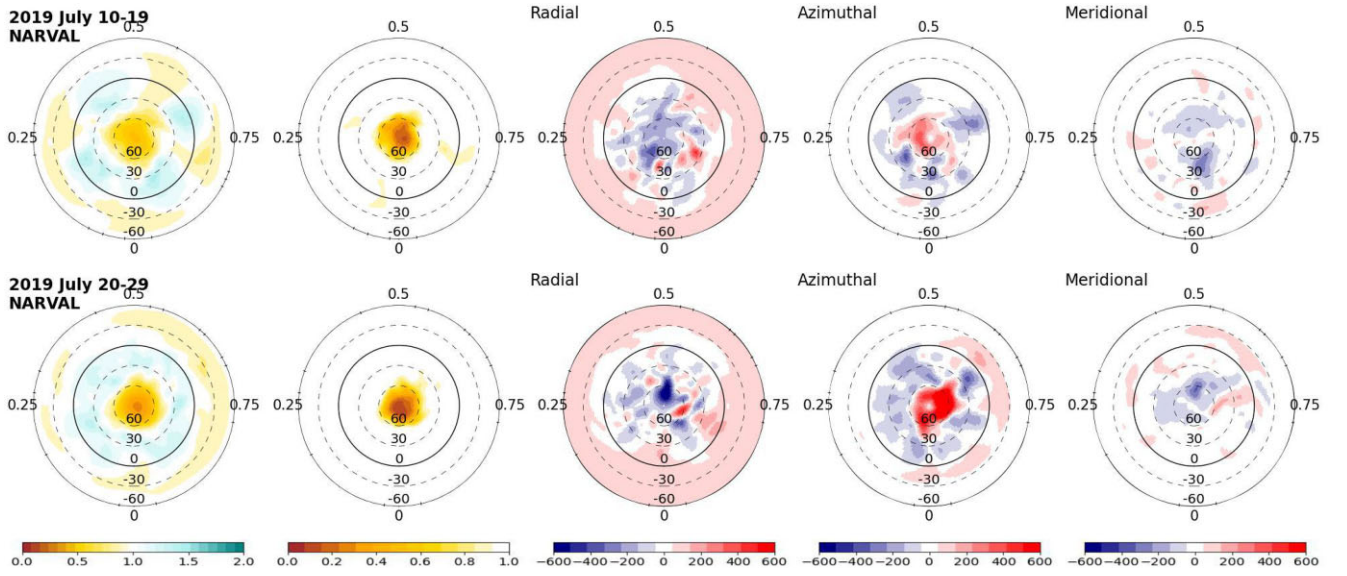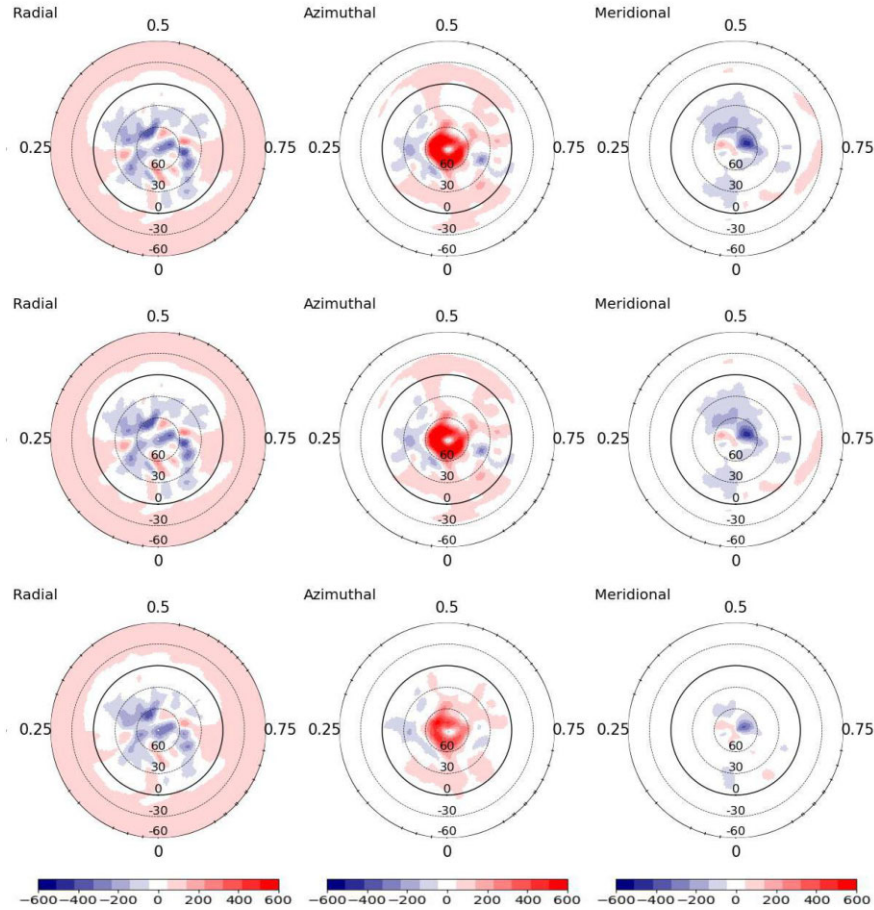**Figure B2.** Same as Fig. B1 but for 2011 May 14–16 through to 2019 June.

Figure B3. Same as Fig. B1 but for 2019 July 10–19 and 2019 July 20–29.

APPENDIX C: IMPACT OF BRIGHTNESS TOPOLOGY AS AN INPUT TO MAGNETIC FIELD MODELLING

Fig. C1 shows the impacts on the final reconstructed magnetic field of using pre-computed DI maps for the magnetic field inversion.

Figure C1. Top: The magnetic field in 2007 May when the brightness + spot model is considered during magnetic field reconstruction. Middle: The magnetic field as shown in Fig. B1 when the spot-only (filling factor) model is considered during magnetic field reconstruction. Bottom: The magnetic field when no brightness model is considered in the reconstruction of the magnetic model. The azimuthal and meridional fields are clearly weaker when the presence of the dark polar spot is not considered in the magnetic field reconstruction. There is minimal difference in the radial magnetic field reconstruction across the three models. There is also minimal difference in the three reconstructed field components when using the brightness + spot or the spot-only models as input for the field reconstruction.

APPENDIX D: RESULTS OF RV ACTIVITY FILTERING - GPR METHOD

Figs D1–D3 show corner plots indicating the posterior distributions and best-fitting parameters for a quasi-periodic GP fitted to various sets of RV observations.

Fig. D1 (left) shows the corner plot for 2007 May when using a logarithmic prior for θ_2. The logarithmic prior allows for greater exploration of short length scales. In practice, this resulted in the decay parameter converging toward the lower edge of the prior (i.e. toward zero, see Fig. D1) such that the final numerical model did not represent a realistic physical solution. With a uniform prior (right),

θ_2 did not converge to a unique solution, regardless of the upper limit of the prior. Without any strong evidence for the mean or standard deviation of the spot decay time-scale, we avoided using an informative Gaussian prior for θ_2, which would bias the model and artificially boost the posterior likelihood.

Fig. D2 shows the posterior distributions of the model parameters for the combined HARPS data using two different priors for θ_2. On the left, the GP converges toward a short decay time-scale of ~ 9 d, which may be related to the lengths of individual observing runs. On the right the value for θ_2 is larger than the total length of the data (~ 1130 d), and is possibly tied to the long-lived polar spot which is present for the entire data set.
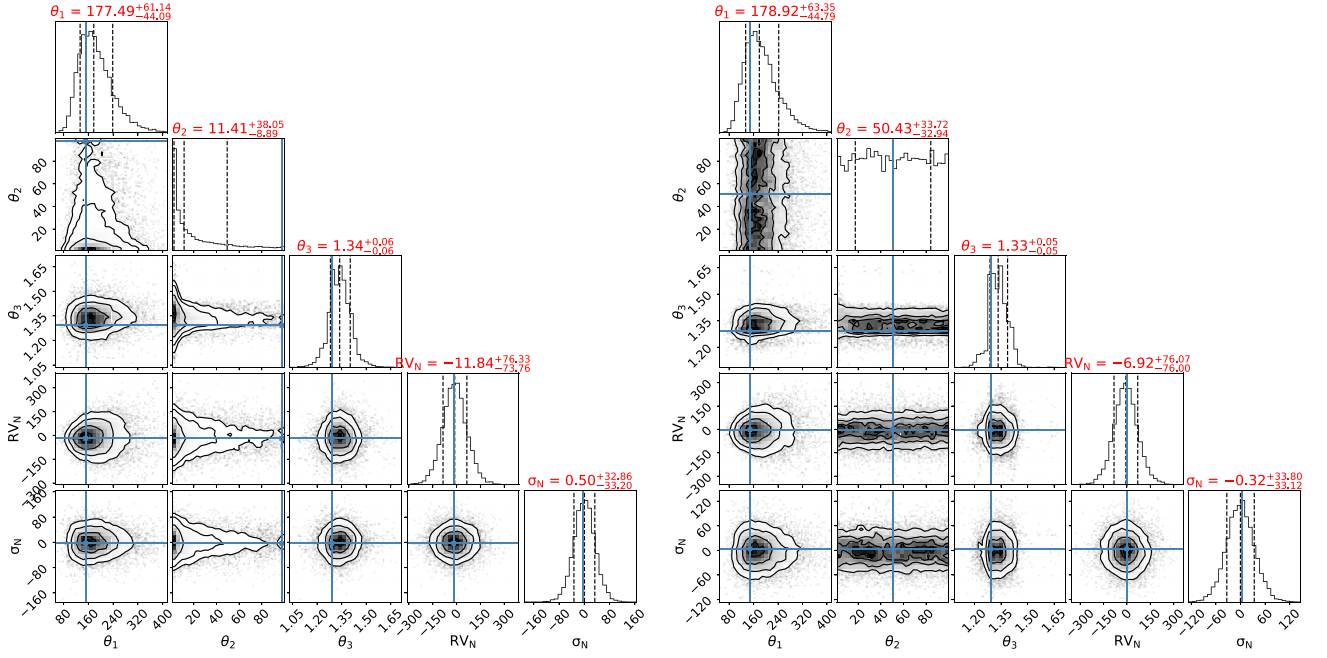
Figure D1. Posterior distribution of the fitted parameters for an activity-only model to the RVs for 2007 May. Left: the priors for each parameter are as per Table 3. Right: the priors for θ_2 are $\mathcal{U}$ (1.33, 100). The blue lines indicate the most likely set of parameters for the GP and dashed vertical lines in the histograms are the 0.16, 0.50, and 0.84 quantiles. Contours are 1-σ, 2-σ, and 3-σ levels.
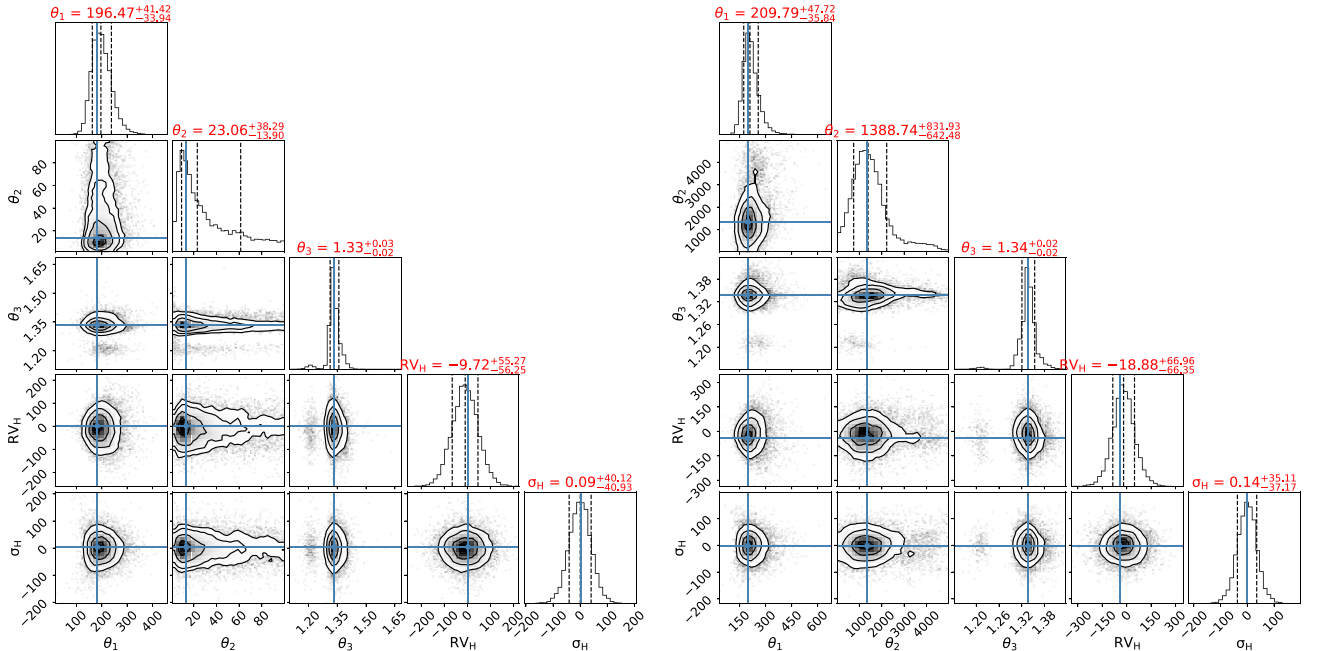
Figure D2. Posterior distribution of the fitted parameters for an activity-only model to the RVs for HARPS data (2010 August to 2013 September). Left: the priors for each parameter are as per Table 3, and the marginal likelihood for this model is $lnZ = -226.5$. Right: the priors for θ_2 are $\mathcal{U}$ (1.33, 5000) and the marginal likelihood for this model is $lnZ = -225.2$.
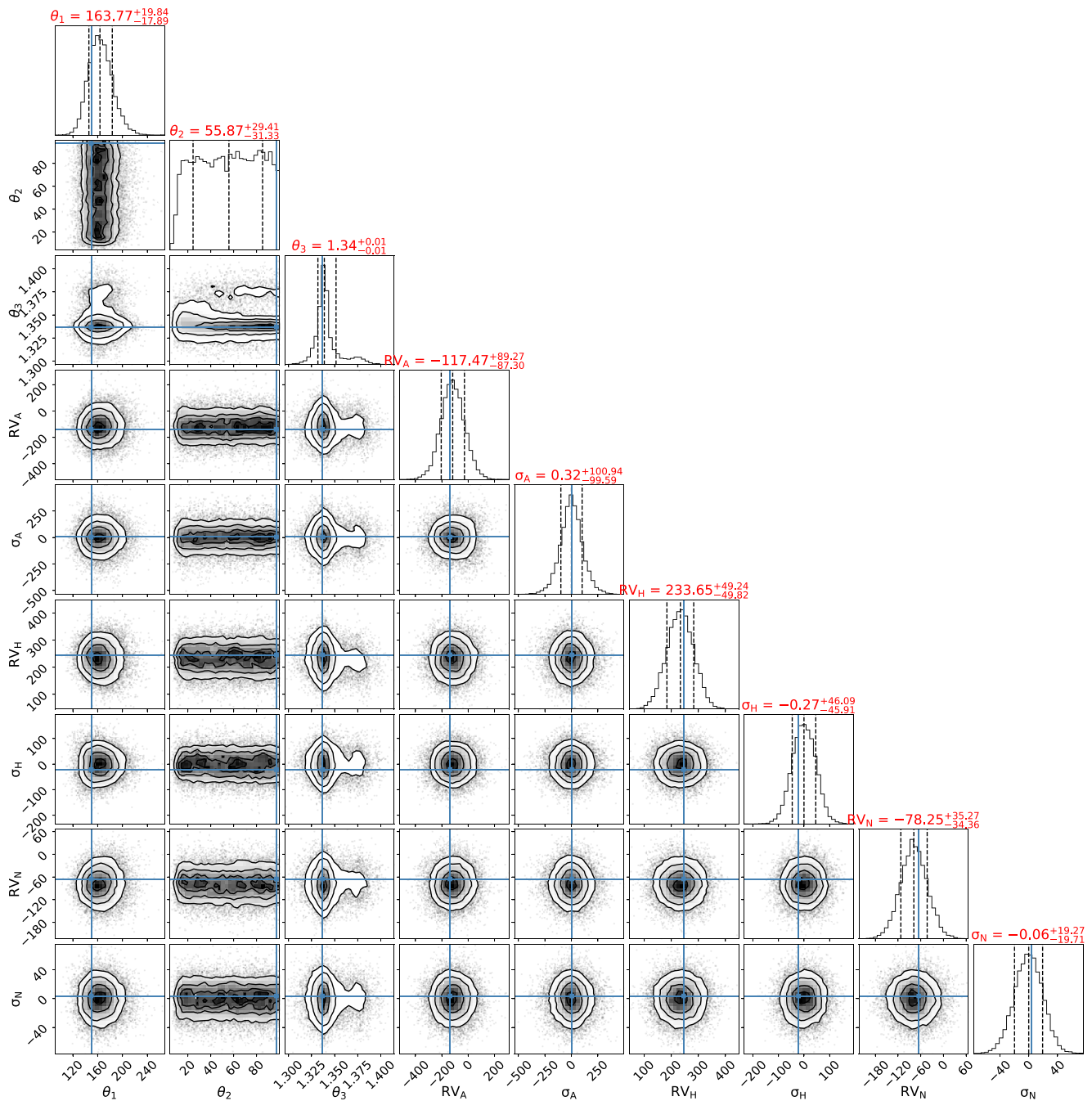
Figure D3. Posterior distribution of the fitted parameters for an activity-only model to the entire set of RVs, from 2004 September through to 2019 July 20–29.

This paper has been typeset from a TEX/LATEX file prepared by the author.